2010-01-0338
SAND2009-6828C

Ethanol Autoignition Characteristics and HCCI Performance for Wide Ranges of Engine Speed, Load and Boost

Magnus Sjöberg and John E. Dec
Sandia National Laboratories

ABSTRACT

The characteristics of ethanol autoignition and the associated HCCI performance are examined in this work. The experiments were conducted over wide ranges of engine speed, load and intake boost pressure (P_{in}) in a single-cylinder HCCI research engine (0.98 liters) with a CR = 14 piston.

The data show that pure ethanol is a true single-stage ignition fuel. It does not exhibit low-temperature heat release (LTHR), not even for boosted operation. This makes ethanol uniquely different from conventional distillate fuels and offers several benefits: a) The intake temperature (T_{in}) does not have to be adjusted much with changes of engine speed, load and intake boost pressure. b) High P_{in} can be tolerated without running out of control authority because of an excessively low T_{in} requirement.

However, by maintaining true single-stage ignition characteristics, ethanol also shows a relatively low temperature-rise rate just prior to its hot ignition point. Therefore, ethanol does not tolerate as much combustion-phasing retard as fuels that exhibit LTHR and/or pronounced intermediate-temperature heat release. Since combustion retard is important for avoiding excessive pressure-rise rates, the distinct single-stage ignition characteristic of ethanol can be considered a drawback when reaching for higher loads. Nonetheless, an $IMEP_g$ of 11.3 bar was demonstrated for P_{in} = 247 kPa.

Finally, the latest ethanol chemical-kinetics mechanism from the National University of Ireland – Galway was evaluated against the experimental engine data using a multi-zone model. Overall, the mechanism performs very well over wide ranges of operating conditions.

INTRODUCTION

The homogeneous charge compression ignition (HCCI) combustion process offers good fuel economy and very low nitrogen-oxide (NO_x) and particulate emissions. Therefore, HCCI combustion is one option for improving the efficiency of the spark-ignited gasoline engine. HCCI is also pursued in order to reduce the requirement for NO_x aftertreatment in the latest generation of compression-ignited diesel engines. However, several technical hurdles need to be overcome before HCCI can be broadly applied in production engines. For example, controlling the combustion phasing and increasing the power output while maintaining acceptable pressure-rise rate (PRR) are two important research areas.

The autoignition reactivity of the fuel is a very important parameter impacting the fuel's potential suitability for an HCCI combustion system. This is particularly important to consider for emerging alternative fuels, whose reactivities can vary greatly [1]. If the fuel has high resistance to autoignition (*i.e.* high octane number), high charge temperatures are required during the compression stroke in order to ensure autoignition. This can pose a problem for low-load operation since the available exhaust heat may be insufficient for raising the temperature of the fresh charge to the required level [2]. Also, a higher intake temperature (T_{in}) leads to lower charge density for a given intake pressure (P_{in}), which typically has a negative influence on the peak load that can be obtained [3,4]. In addition, the high temperature required for autoignition also leads to high peak-combustion temperatures, so excessive NO_x can become the load-limiting factor, even for well-mixed "classical" HCCI [3].

On the other hand, if the fuel is very prone to autoignite (*i.e.* has a low octane number), the lowest possible T_{in} in combination with large quantities of exhaust-gas recirculation (EGR) may be required to obtain an acceptable 50% burn point (CA50), typically at or slightly after TDC. Since EGR gases displace air, the intake mole fraction of oxygen, $[O_2]$, is reduced with increasing amount of EGR. Therefore, the load-limiting factor for very reactive fuels can be oxygen deprivation [3]. Also, if the fuel is very reactive, it may not be suitable for use in combustion systems that revert to SI operation for parts of the load/speed range. This is because high resistance to autoignition (*i.e.* high octane number) is required to avoid engine knock for SI operation, particularly for engines that employ intake-pressure boost [5].

Worldwide, the most widespread alternative fuel for light-duty engines is currently ethanol. The most common production methods are based on fermentation of corn or sugarcane. In addition, many predictions suggest that cellulosic ethanol has the potential to increase ethanol production substantially. Practically all gasoline SI engines tolerate some fraction of ethanol in the fuel (~10%), and most SI engines are readily adapted for operation on fuels that contain up to 85% ethanol (*i.e.* flex-fuel engines) [5]. Based on the importance of ethanol as an alternative fuel and the current trend towards more advanced and efficient engines, it is important to fully understand the characteristics of ethanol when used in advanced combustion systems for internal combustion engines. A literature search shows that a number of studies of ethanol HCCI combustion have been conducted [*e.g.* 6,7,8]. Jointly, these studies cover rather wide ranges of operating conditions. However, because of differences in engine geometry, how the engines were operated, and how the data are presented, it is very hard to form a comprehensive view of the autoignition characteristics of ethanol for HCCI operation. The current study tries to fill this apparent gap in the literature.

Furthermore, modeling of the combustion processes is often considered a key element when developing advanced engines. Because of this, it is important that well validated chemical-kinetics mechanisms be available. This is particularly true for emerging alternative fuels, which may have characteristics that differ substantially from traditional fuels like gasoline. Therefore, the current study evaluates the fidelity of a newly developed ethanol mechanism.

SCOPE AND OBJECTIVES

The primary objective of this study is to experimentally investigate the autoignition behavior of ethanol under HCCI conditions across relatively wide ranges of operating conditions. Integral to this assessment are comparisons of the autoignition and heat-release characteristics of ethanol to those of other (non-oxygenated) fuels. The second objective is to assess the fidelity of a newly developed chemical-kinetics mechanism for ethanol. This is done by detailed comparisons of multi-zone model predictions with the acquired engine data.

First, the experimental setup, data acquisition and analysis are described. This is followed by a description of the chemical-kinetics mechanism and the model setup. The results are then divided into five main parts:

1. Combustion-phasing sweep by changing T_{in} at $\phi = 0.40$, 1200 rpm, and $P_{in} = 100$ kPa.
2. Engine-speed sweep at $\phi = 0.38$, $P_{in} = 100$ kPa, while holding CA50 = 372°CA by adjusting T_{in}.
3. Fuel/air-equivalence ratio (ϕ) sweep to detect CA10 changes at $T_{in} = 143$°C, $P_{in} = 100$ kPa and 1200 rpm.
4. Intake-boost pressure sweep at $\phi = 0.40$, 1200 rpm, while holding the 10% burn point (CA10) = 369.0°CA by adjusting T_{in}.
5. Demonstration of high $IMEP_g$ for boosted operation at 1200 rpm, using a lower $\phi = 0.36$ and $P_{in} = 247$ kPa.

The evaluation of the chemical-kinetics mechanism for ethanol is performed in conjunction with each of the parameter sweeps in parts 1 – 4 above.

EXPERIMENTAL SETUP

The engine used for this study is based on a Cummins B-series diesel engine, which is a typical medium-duty diesel engine with a displacement of 0.98 liters/cylinder. A schematic of the setup is shown in Fig. 1. The configuration of the engine and facility is the same as for recent studies (*e.g.* Ref. [3]).

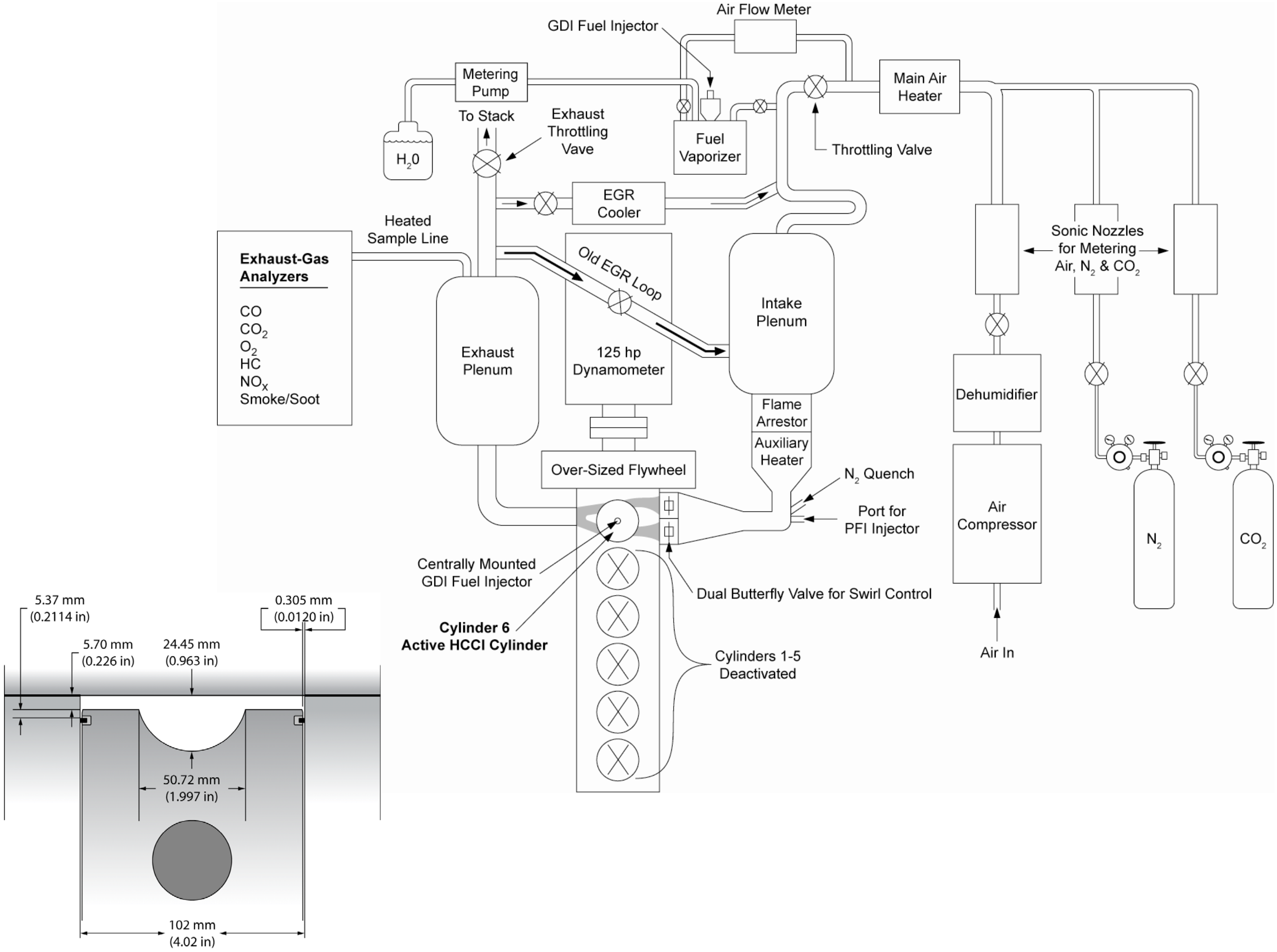

Figure 1. Schematic of the HCCI engine facility, and combustion-chamber dimensions at TDC with the CR = 14 piston.

Furthermore, the schematic in Fig. 1 shows that the piston used for these experiments with ethanol, iso-octane and gasoline provides an open combustion chamber with a large squish clearance and a quasi-hemispherical bowl. The geometry renders a geometric compression ratio (CR) of 14:1. The bowl of this piston is deeper than the shallow scallop design used in several previous publications (*e.g.* Ref. [4]). In particular, all data with PRF80 fuel that are presented here were acquired with a CR = 14 piston that has a more shallow piston bowl. However, comparative measurements show that both the T_{in} requirements and the heat-release rate (HRR) are nearly identical, regardless of piston-bowl geometry. Thus, the results for PRF80 can be directly compared with those of the other three fuels in this study. Finally, note that the custom-design piston provides a small topland-ring crevice, amounting to only 2.1% of the top-dead-center (TDC) volume, including the volume above and behind the top piston ring.

For all operating conditions of this study, the engine was fueled using a fully premixed fueling system featuring an electrically heated fuel vaporizer (Fig. 1). The intake air was metered with a sonic nozzle. A main air heater and tank heaters (not shown) were used to preheat the mixture of air and fuel. An auxiliary air heater mounted close to the engine was used to precisely control the intake temperature of the inducted charge. For all operating conditions, the exhaust back pressure was kept at atmospheric level by maintaining a fully open exhaust throttling valve. Engine specifications are listed in Table 1. A detailed description of the engine modifications for HCCI operation can be found in Ref. [9].

TABLE 1. Engine Specifications

Displacement (single-cylinder)	0.981 liters
Bore	102 mm
Stroke	120 mm
Connecting Rod Length	192 mm
Nominal Geometric Compression Ratio	14:1
No. of Valves	4
IVO	0°CA*
IVC	202°CA*
EVO	482°CA*
EVC	8°CA*
Intake Air Swirl Ratio, Both Ports Combined	0.9

* Valve closing and opening timings refer to 0.1 mm lift.

Intake temperatures were monitored using thermocouples mounted in the two intake ports close to the cylinder head. Firedeck temperatures were monitored with a thermocouple embedded in the cylinder head so that its junction was about 44 mm off the cylinder center and 2.5 mm beneath the surface. Surface temperatures were estimated by extrapolating the thermocouple reading to the surface, using the thickness of the firedeck and assuming that its back surface was at the 100°C cooling-water temperature.

Cylinder pressure measurements were made with a transducer (AVL QC33C) mounted in the cylinder head approximately 42 mm off center. The pressure transducer signals were digitized and recorded at ¼° crank angle (CA) increments for at least 100 consecutive cycles per data point. To compute the PRR, each individual cycle is first low-pass filtered (< 2.5 kHz, see Ref [9]) and then analyzed with a linear fit over a moving ±0.5°CA window to extract the maximum PRR. The reported PRRmax values are computed by averaging the PRRs of at least 100 individual cycles. Similarly, the 50% burn point (CA50) was first computed from the low-pass-filtered pressure trace for each individual cycle (without heat-transfer correction), and then averaged. However, it should be noted that for operation with fuels that show LTHR, the LTHR is excluded when the cumulative heat release is computed. Effectively, the reported CA50 for operating points with LTHR refers to 50% burn point for the main combustion event, starting at the crank angle of minimum heat-release rate between the low- and high-temperature combustion events. Referring to the main combustion event alone is considered more relevant for quantifying the main-combustion timing. Note that intermediate-temperature heat-release (ITHR) occurs just before the hot-ignition point, so the ITHR will be included as a part of the main combustion event both for fuels with and without LTHR.

A second method of computing the HRR was used for the presented HRR traces. Here, the heat-release rate was computed in a more refined way from the ensemble-averaged pressure trace (with the 2.5 kHz low-pass filter applied), using the Woschni correlation for heat transfer [10].

Charge temperatures during the closed part of the cycle (*i.e.* compression/expansion) are computed using the ideal-gas law in combination with the measured pressure (ensemble-averaged over 100 cycles), the known cylinder volume, and the trapped mass. The trapped mass equals the sum of the supplied air, fuel, and residuals, the latter being computed by applying the ideal gas law to the clearance volume at TDC-valve-overlap, using a pressure that was determined from cycle-simulation modeling (using Ricardo's WAVE program) and an estimated residual temperature based on exhaust blowdown to this pressure. The average molecular weight used for the calculation of the charge temperature during the compression stroke corresponds to that of the trapped gases - including fresh air, retained residuals, and fuel. During the combustion event, and in proportion to the mass fraction burned, the molecular weight in the calculations is gradually changed to that of the measured exhaust composition. This exhaust molecular weight is then used for the remainder of the expansion stroke and for computing the trapped mass.

Exhaust emissions data were also acquired, with the sample being drawn from the exhaust plenum using a heated sample line (see Fig. 1). For all conditions, the levels of CO, CO_2, HC, NO_x, O_2 were measured using standard exhaust-gas analysis equipment as shown in Table 2. Since the fuel is oxygenated, a separate test was performed to check the response of the HFID to ethanol. It was found that the carbon-atom-detection efficiency was 65%. Accordingly, the HC emissions reported here have been multiplied by 1.53 to correct for this, with the assumption that the HFID response is dominated by ethanol molecules in the exhaust [11]. Initial measurements with the smoke meter showed that the smoke levels were virtually zero since the fuel was well mixed with the air. Therefore, smoke was not measured for all data points.

TABLE 2. Emissions Analysis Equipment

CO	Non-Dispersive Infrared Detector, Rosemount 880A
CO_2	Non-Dispersive Infrared Detector, CAI 602 NDIR
HC	Heated Flame Ionization Detector (HFID), CAI 600 HFID
NO_X	Chemiluminescence Analyzer, Rosemount 951A
O_2	Paramagnetic Analyzer, Rosemount 755R
Smoke	Optical-Density of Filter Paper, AVL415S

Because HCCI combustion is very sensitive to temperature, the engine coolant and oil were both fully preheated to 100°C before starting the experiments. For all data presented, 0°CA is defined as TDC intake (so TDC compression is at 360°). This eliminates the need to use negative crank angles or combined bTDC, aTDC notation.

The fuels used for this study are neat (100%) ethanol, iso-octane, gasoline, and PRF80 (an 80/20 blend of the primary reference fuels, iso-octane and n-heptane). All of these fuels are fairly volatile, and this facilitates the charge preparation process. Table 3 shows the fuel compositions and other relevant parameters. It can be noted that the mass-based heating value of ethanol is substantially lower than the other fuels since ethanol is oxygenated. However, the stoichiometric air/fuel-ratio is also lower for ethanol. Consequently, for the same ϕ, the heating values of the fuel/air-mixtures are nearly identical for the four fuels. Since ethanol tends to absorb water from the ambient air, care was taken to minimize the exposure of the ethanol to the ambient air by keeping fuel containers sealed and to displace air with nitrogen gas above the fuel in the fuel tank.

TABLE 3. Fuel Properties

Fuel:	Ethanol	Iso-Octane	Gasoline	PRF80
Iso-Octane %vol.	0	100	Unknown	80
n-Heptane %vol.	0	0	Unknown	20
Saturates %vol.	100	100	73.1	100
Olefins %vol.	0	0	4.2	0
Aromatics %vol.	0	0	22.7	0
RON	107	100	90.8	80
MON	89	100	83.2	80
Antiknock Index (RON+MON)/2	98	100	87.0	80
C-atoms	2	8	6.78	7.78
H-atoms	6	18	13.6	17.56
O-atoms	1	0	0	0
Molecular weight	46.07	114.2	95.2	111.1
A/F Stoichiometric	9.00	15.13	14.8	15.14
Lower heating value for gas-phase fuel [MJ/kg]	27.75	44.65	43.17	44.71
Lower heating value for stoichiometric charge [MJ/kg]	2.775	2.769	2.734	2.770

CHEMICAL-KINETICS MODELING SETUP

The chemical-kinetic modeling approach used in this work is similar to one used previously by the authors [12]. The calculations were carried out using a special multi-zone version of the Senkin application of CHEMKIN III developed at Sandia [13,14]. The model treats each zone as a single lumped mass with uniform composition and thermodynamic properties. The chemistry is treated independently for each zone. The only coupling between zones is the pressure, which is assumed to equilibrate instantaneously as heat is released in any of the zones. The total volume of all zones is modeled according to the standard slider-crank relationship [10], using the geometry and specifications of the Sandia HCCI research engine shown in Table 1. As a result, the volume of each zone effectively depends on its mass and temperature relative to the other zones. The number of zones and the thermal distribution are described in the in Appendix A, which also includes a comparison with single-zone modeling.

A newly developed reaction mechanism for ethanol is used [15]. The ethanol mechanism has 58 species and 310 reactions. It is developed to be an integrated part of a gasoline surrogate mechanism [16]. This much larger surrogate mechanism is a joint effort between the National University of Ireland (NUI) – Galway (Curran, Serinyel, and Metcalfe) and Lawrence-Livermore National Lab (LLNL) (Pitz and Mehl).

For simplicity, heat transfer effects were not modeled. However, to ensure a charge-pressure history during the compression stroke that is very similar to that of the experiment, the model was set up with CR = 12.8. This is somewhat lower than the nominal CR = 14 used in the experiment.

The amount and composition of the reactants were computed based on careful analysis of the engine experiment, including emissions measurements. The air was modeled using the correct proportions of N_2, O_2 and CO_2, where atmospheric argon was lumped as atmospheric N_2. The residuals were modeled using CO_2, H_2O, N_2, CO, unburned fuel, and air. For this modeling work, no attempt was made to capture the effect of partially burned fuel that is encountered experimentally in residuals, and so the measured exhaust hydrocarbon mole fraction was converted to an ethanol mole fraction in the residuals. It should be noted that the amount of residuals is low as a result of the use of conventional valve timings. In this study, the residual mass fraction ranges from 2.1% to 5.8%, depending on the boost pressure, engine speed, and residual temperature.

RESULTS

As described in conjunction with Fig. 1, a CR = 14 piston was installed for all tests. However, the choice of compression ratio influences the T_{in} requirements, thus affecting the performance of a given fuel [3,17,18]. This should be considered when comparing the data presented here with data acquired in other engines using different compression ratios.

COMBUSTION-TIMING SWEEP / T_{IN}-SENSITIVITY

This section deals with the use of T_{in} adjustments to control the combustion phasing for a fixed engine speed of 1200 rpm and P_{in} = 100 kPa. Precise CA50 control is particularly important at high loads, since too-advanced CA50 can lead to excessive PRR and engine knock [19]. Below, the degree of response of the combustion phasing to a change of T_{in} will be referred to as T_{in} sensitivity.

Figure 2 shows how the T_{in} has to be adjusted to achieve a certain CA50 for ethanol, iso-octane and PRF80. Directly relevant is Fig. 3, which shows that both ethanol and iso-octane exhibit single-stage ignition behavior without LTHR. As a result, their T_{in} requirements are comparable. Even so, Fig. 2a shows that iso-octane requires more than 33°C higher T_{in} than ethanol for this range of CA50. This shows that ethanol has a higher autoignition reactivity than iso-octane under these conditions (1200 rpm and P_{in} = 100 kPa). The term autoignition reactivity will be used extensively throughout the paper and refers to how easy it is to achieve autoignition for the fuel in question. For operation with a constant CR, low residual fraction, and no EGR - as in this study - the autoignition reactivity is quantified by the required T_{in} to achieve autoignition. A fuel with high reactivity requires low T_{in} whereas a fuel with low reactivity requires high T_{in}. In contrast to ethanol and iso-octane, PRF80 requires a much lower T_{in}, so it is plotted by itself in Fig. 2b. Under these operating conditions, PRF80 exhibits LTHR, as illustrated in Fig. 3, and this explains why its T_{in} has to be low.

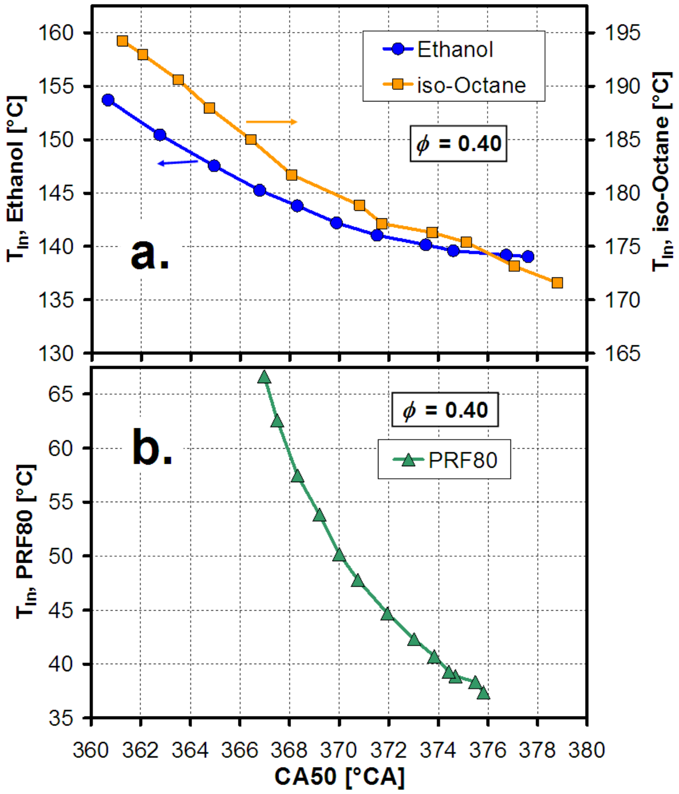

Figure 2. Required T_{in} as a function of desired CA50 for ethanol, iso-octane, and PRF80. $\phi = 0.40$, 1200 rpm, and P_{in} = 100 kPa.

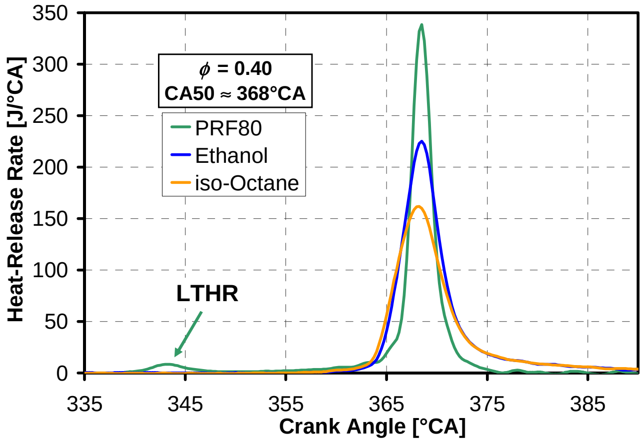

Figure 3. HRR traces for ethanol, iso-octane, and PRF80. CA50 ≈ 368°CA, $\phi = 0.40$, 1200 rpm, and P_{in} = 100 kPa.

Not only are the T_{in} requirements different between the fuels, the slope of the curves in Fig. 2 are different as well. PRF80 has the steepest slope, so among these fuels its combustion phasing has the lowest sensitivity to changes of T_{in}. Its low T_{in} sensitivity can be explained by its LTHR in combination with enhanced ITHR [4]. Figure 3 clearly shows the LTHR, and Fig. 4 zooms in on the ITHR that precedes the main combustion. The presence of LTHR reduces the sensitivity of the autoignition timing to changes of the charge temperature because the amount of LTHR increases with decreasing T_{in}, thus counteracting the direct influence of changes in T_{in} on the charge temperature at TDC. The enhanced ITHR in the 350 - 363°CA range (see Fig. 4) increases the temperature-rise rate (TRR) just before the hot-ignition point, as Fig. 5 shows. As explained in detail in [4], with a higher TRR, the timing of transition into hot ignition becomes less sensitive to changes of the charge temperature. Consequently, the higher TRR due to enhanced ITHR contributes to the low T_{in} sensitivity for PRF80, as Fig. 2b shows.

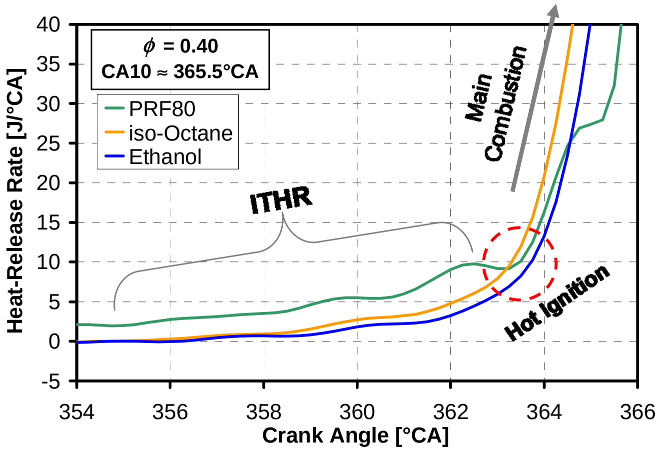

Figure 4. HRR during the early part of the autoignition event for ethanol, iso-octane, and PRF80. CA10 ≈ 365.5°CA, ϕ = 0.40, 1200 rpm, and P_{in} = 100 kPa.

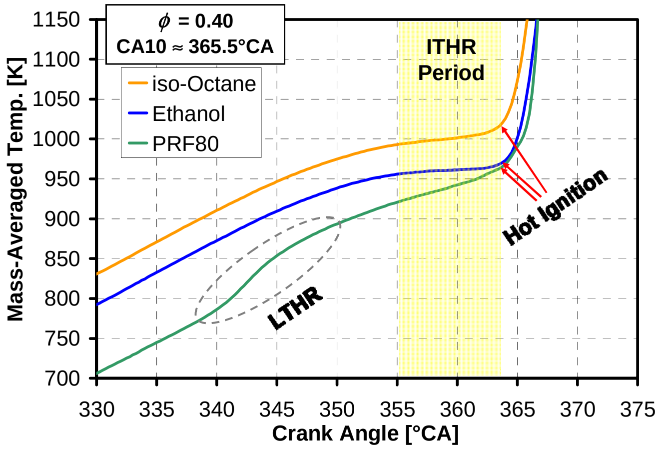

Figure 5. Temperature rise during the late compression stroke and early part of the autoignition event for ethanol, iso-octane, and PRF80. CA10 ≈ 365.5°CA, ϕ = 0.40, 1200 rpm, and P_{in} = 100 kPa.

In contrast, Fig. 2 shows that the CA50 of both ethanol and iso-octane are much more sensitive to changes of T_{in}. Neither ethanol nor iso-octane exhibit LTHR and Fig. 4 shows much less ITHR for these fuels. Consequently, the TRR prior to hot ignition is also much lower, as can be seen in Fig. 5. When the hot-ignition temperature is approached with a shallow slope (*i.e.* low TRR), the crank angle of transition to hot ignition becomes very sensitive to changes of charge temperature (vertical displacement of the temperature trace). This explains the higher T_{in} sensitivity. Examination of Fig. 2a reveals that ethanol has a slightly higher T_{in} sensitivity than iso-octane. This is consistent with the somewhat lower ITHR and TRR prior to the hot ignition.

In this sense, ethanol is a more pronounced single-stage-ignition fuel than iso-octane. This could make it harder to control the combustion timing for operation with retarded combustion phasing using ethanol.

It is important to maintain stable combustion with low cycle-to-cycle variations. This can be an issue for operation with more retarded combustion phasing. Figure 6 shows the standard deviation of $\mathrm{IMEP_g}$ as a function of CA50 for ethanol, iso-octane and PRF80. All fuels exhibit larger variations with increasing CA50 retard. As explained in Ref. [4], this happens because the TRR becomes lower with CA50 retard as the piston-expansion cooling becomes more rapid for later crank angles. With a lower TRR, the onset of hot ignition becomes more sensitive to cycle-to-cycle variations of the charge temperature, as exemplified in Fig. 7, which is reproduced from Ref. [4]. Associated with larger variations of the hot-ignition timing are also larger variations of $\mathrm{IMEP_g}$. In Fig. 6, the curves for ethanol and iso-octane are nearly overlapping. With a 2% limit of tolerable $\mathrm{IMEP_g}$ variations, this means that both these single-stage ignition fuels have an identical CA50 retard limit of 373°CA. Based on their similar TRR prior to hot ignition, it could have been expected that the CA50 retard limit be similar. However, since Fig. 5 shows that ethanol has slightly lower TRR, it would also be expected that ethanol would tolerate slightly less CA50 retard. This slight inconsistency is believed to be related to the somewhat higher $\mathrm{IMEP_g}$ that ethanol produces, as will be shown below. It should be remembered that Fig. 6 compares $\mathrm{IMEP_g}$ variations, not variations of the autoignition timing.

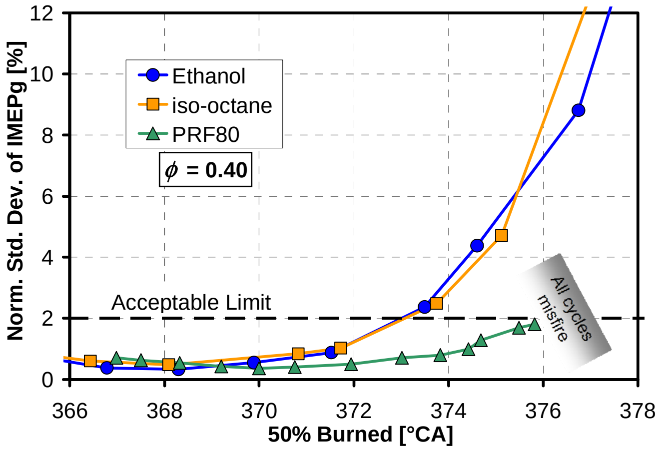

Figure 6. Standard deviation of $\mathrm{IMEP_g}$ normalized by ($\mathrm{IMEP_g}$-$\mathrm{IMEP_{g,motored}}$) as a function of CA50 for ethanol, iso-octane, and PRF80. $\phi = 0.40$, 1200 rpm, and P_{in} = 100 kPa.

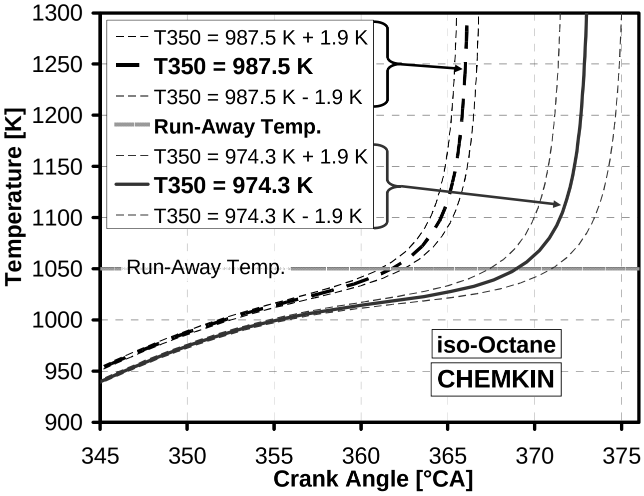

Figure 7. CHEMKIN predictions of the influence of ±1.9K variations of compressed gas temperature at 350°CA on the timing of hot ignition, for two different baseline combustion phasings. Iso-octane. Reproduced from Ref. [4].

In contrast, PRF80 shows substantially lower cycle-to-cycle variations of $\mathrm{IMEP_g}$ in the 370 - 376°CA range. This is in agreement with its much higher TRR prior to the hot-ignition point, and is an advantage for PRF80. However, as annotated in Fig. 6, if CA50 is retarded beyond 376°CA all cycles tend to misfire after the first misfire cycle occurs. This is a drawback associated with the use of PRF80. The single-stage fuels do not tend to “fall off the edge” like PRF80, and can therefore recover stable combustion more easily after a misfire cycle has occurred. These phenomena are discussed in detail in Ref. [4].

One particular reason for retarding CA50 is to control the $\mathrm{PRR_{max}}$. Indeed, Fig. 8 shows that CA50 retard is effective for reducing the $\mathrm{PRR_{max}}$ for all these fuels. Retarding the combustion phasing amplifies the benefit of the existing thermal stratification, leading to a longer combustion duration. In addition, having the combustion take place away from TDC reduces the total pressure rise associated with the combustion since the in-cylinder volume is larger than at TDC. Also, ongoing heat transfer can cause the charge be more thermally stratified during the combustion event when the start of combustion is delayed. These beneficial effects of combustion-phasing retard are explained in detail in Ref. [3], with supporting modeling work in Refs. [12,19]. Imaging of in-cylinder thermal stratification in the corresponding optical engine can be found in Ref. [20].

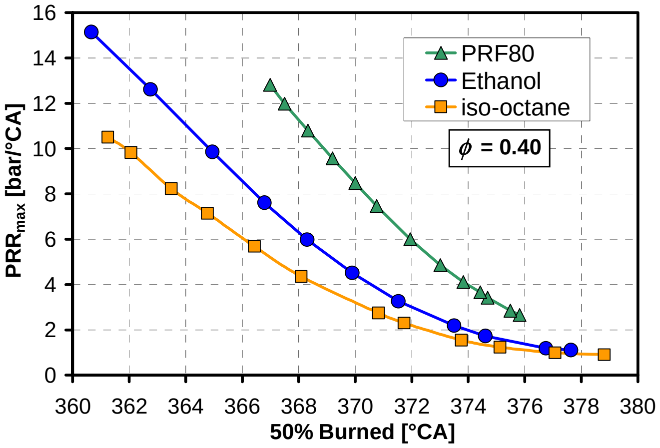

Figure 8. PRR$_{max}$ as a function of CA50 for ethanol, iso-octane, and PRF80. $\phi = 0.40$, 1200 rpm, and P_{in} = 100 kPa.

Figure 9 shows the IMEP$_g$ for the three fuels. There are substantial differences between the fuels. PRF80 exhibits the highest power output and iso-octane the lowest, with ethanol in between. This happens because P_{in} was maintained at 100 kPa and ϕ at 0.40. Since a higher T_{in} lowers the charge density, less charge mass is inducted for each intake stroke. Since $\phi = 0.40$ for all fuels, this also means that less fuel energy is inducted for operation with higher T_{in}.

These variations of IMEP$_g$ can explain the differences in PRR between the fuels. Figure 8 shows that the PRR$_{max}$ varies substantially between the three fuels. For a given CA50, PRF80 has the highest PRR$_{max}$, and also the highest IMEP$_g$. Conversely, iso-octane has the lowest IMEP$_g$, and also shows the lowest PRR$_{max}$, corresponding to a lower amount of inducted fuel energy. Ethanol consistently falls in between iso-octane and PRF80 in both Fig. 8 and Fig. 9. It should be noted that PRR$_{max}$ > 9 bar/°CA for several of the data points in Fig. 8. These high values of PRR$_{max}$ should normally be avoided since they lead to in-cylinder ringing/knock and enhanced heat-transfer losses, which reduces the thermal efficiency of the engine.

Furthermore, it can be seen in Fig. 9 that CA50 influences the IMEP$_g$ for all fuels. For ethanol and iso-octane, the highest IMEP$_g$ is found in the 368 - 370°CA range, whereas PRF80 exhibits the highest IMEP$_g$ in the 371 - 375°CA range. For all fuels, the IMEP$_g$ drops for the more advanced data points. This happens partly because the higher T_{in} required to advance CA50 reduces the inducted fuel mass, but also because the higher PRR increases convective heat-transfer losses. On the other hand, when CA50 is retarded beyond 372°CA, the IMEP$_g$ starts to drop substantially for both ethanol and iso-octane. This happens mostly because the combustion efficiency goes down with excessive CA50 retard. A reduced expansion ratio also contributes some to the drop of IMEP$_g$. However, PRF80 does not show the same IMEP$_g$ reductions for more retarded CA50. This insensitivity arises partly because PRF80 maintains higher combustion efficiency due to its lower cycle-to-cycle variability (Fig. 6). Also contributing to the low sensitivity of IMEP$_g$ to CA50 retard is the strong reduction of T_{in} with CA50 retard that increases the supplied fuel energy.

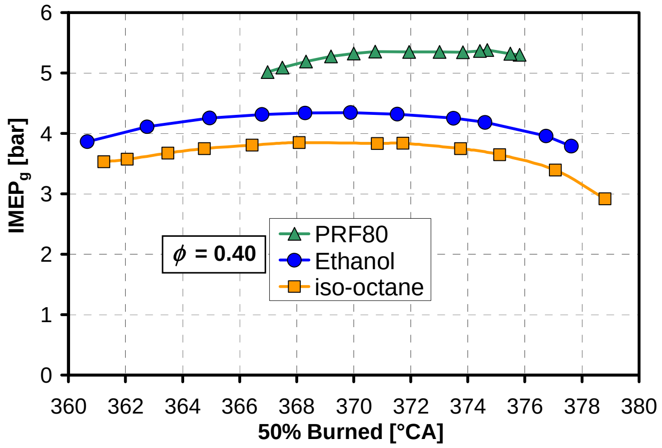

Figure 9. IMEP$_g$ as a function of CA50 for ethanol, iso-octane, and PRF80. $\phi = 0.40$, 1200 rpm, and P_{in} = 100 kPa.

The exhaust emissions of HC and CO for the CA50 sweep are plotted against PRR$_{max}$ in Fig. 10. Note that higher PRR$_{max}$ corresponds to a more advanced CA50, and vice versa. The general trend is that a more complete combustion with higher combustion efficiency is achieved for a more advanced CA50 with higher PRR$_{max}$. This is expected since the peak combustion temperature goes up with a more advanced CA50. The amount of CO is relatively small. At this fairly high ϕ of 0.40, the CO emissions are expected to originate mostly from a thin layer near the combustion-chamber walls where heat-transfer prevents the local combustion temperature from reaching 1500 K, which is needed to complete CO-to-CO$_2$ reactions [21,22,23].

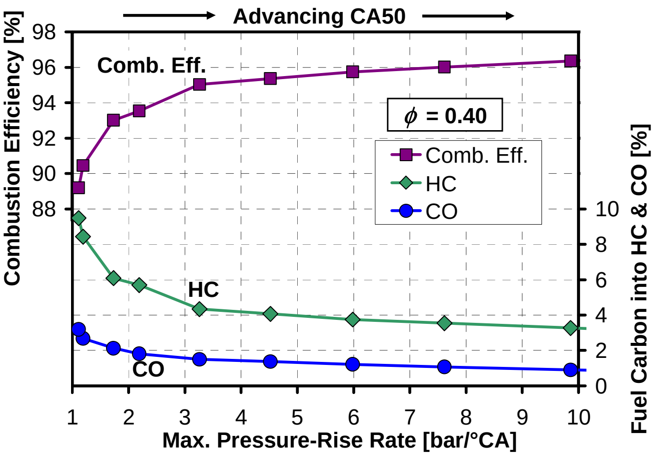

Figure 10. Exhaust emissions of HC and CO as a function of PRR$_{max}$ for ethanol. CA50-sweep with ϕ = 0.40, 1200 rpm, and P_{in} = 100 kPa.

Furthermore, Fig. 10 shows that a larger fraction of the fuel carbon ends up as HC emissions than CO emissions, regardless of PRR$_{max}$ and CA50. It is noteworthy that the HC emissions increase rapidly when CA50 is retarded such that the PRR$_{max}$ becomes lower than 3 bar/°CA. This can be explained as follows. For well-burning and not overly retarded operation at this ϕ of 0.40, HC is expected to originate mainly from crevices [11,23,24,25]. However, with CA50 retard, the PRR$_{max}$ decreases and cycle-to-cycle variations increase.

Consequently, the combustion-induced compression heating of the coldest and not-yet-ignited zones of the in-cylinder charge can become so weak that the hot-ignition temperature is never reached in these zones. In this way, operation with very low PRR_{max} could cause bulk-gas contribution to the HC emissions, particularly from cycles that are more retarded than the average cycle.

Finally, Fig. 11 shows the exhaust emissions of NO_x for ethanol. The NO_x is plotted against the mass-averaged peak-combustion temperature. It can been seen that the NO_x exhaust emissions are very low (1 – 2 ppm) for most data points. This is expected since the fuel and air are well premixed, and ϕ is relatively low. (This low level of NO_x is representative also for most of the ethanol data presented in subsequent sections.) It is only for the two most advanced operating points in the CA50-sweep that a significant amount of NO_x is being produced. This NO_x production correlates with the peak-combustion temperatures exceeding 1920 K. It should be noted that these high-NO_x points also have unacceptably high PRR_{max}, as Fig. 8 shows.

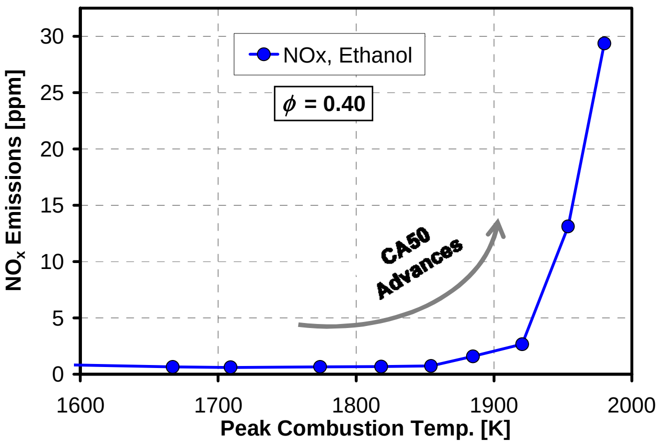

Figure 11. Exhaust emissions of NO_x plotted against peak-combustion temperature for ethanol. CA50-sweep with $\phi = 0.40$, 1200 rpm, and $P_{in} = 100$ kPa.

Modeling of Combustion-Timing Sweep

As mentioned in the Modeling Setup section, the evaluation of the chemical-kinetics mechanism for ethanol was done with a multi-zone model, using a special version of the Senkin application of CHEMKIN. The use of a multi-zone model allows capturing the main effects of the naturally occurring in-cylinder thermal stratification resulting from heat transfer. The selection of temperature spacing between zones is described in Appendix A, which also shows a comparison with single-zone modeling.

Figure 12 shows two experimental pressure traces with two different combustion phasings (curves without symbols). For both of these experimental cases, the crank angle of CA10 is marked with a vertical line. The thermal distribution of the model was fine tuned to provide a good pressure match for the CA10 = 363.2°CA case plotted in Fig. 12. As shown in Appendix A, this matching process resulted in a thermal width at BDC (TW_{bdc}) of 25K for the active (burning) zones of the model. For all subsequent modeling of other conditions, where CA10, engine speed, ϕ, or P_{in} were varied, TW_{bdc} = 25K and thermal distribution were maintained constant. For each experimental operating point, CA10 of the model was made identical to the experimental CA10 by iteratively adjusting the BDC temperature of the hottest zone ($T_{bdc,max}$) to control the combustion phasing. When comparing the model results against the experiment below, it is $T_{bdc,max}$ that is compared against the experimental T_{bdc}. This is justified by the fact that the model and experiment have very similar pressure histories, at least until CA10, as Fig. 12 shows. With a similar pressure history, the hottest zone in the model also has a temperature history that is similar to the hottest (and almost adiabatic [26]) portion of the core of the experiment). No other parameter than $T_{bdc,max}$ was adjusted to match the model CA10 to the experimental CA10, so the resulting predictions of T_{bdc} should provide a fair and consistent assessment of the accuracy of the chemical-kinetics mechanism for ethanol in various HCCI operating regimes.

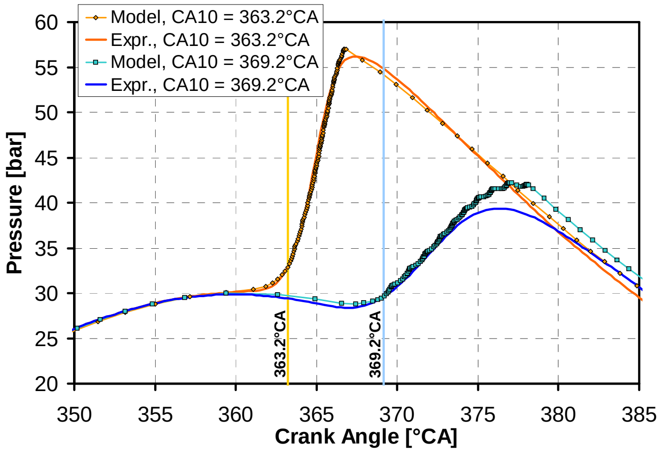

Figure 12. Comparison of pressure traces for the model and experiment using ethanol. ϕ = 0.40, 1200 rpm, and P_{in} = 100 kPa.

Figure 13 compares the T_{bdc} requirement between the model and the experiment. First of all, it should be noted that the experimental T_{bdc} differs from the T_{in} plotted in Fig. 2. The difference arises because of heat transfer between the gas and the surfaces in both the intake port and cylinder during the intake stroke. Dynamic heating during the cylinder-fill process and mixing with hot residual gases also influence the gas temperature, as discussed in detail in Ref. [27]. The experimental T_{bdc} was computed by following the methodology presented in Ref. [27], using measurements of air and fuel flow, P_{in}, and in-cylinder pressure at exhaust valve opening (EVO), in combination with Wave modeling of dynamic heating and pressure at TDC overlap.

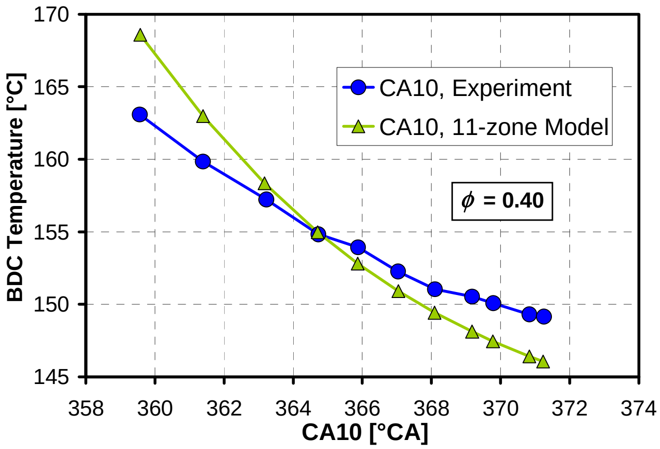

Figure 13. Comparison of the ethanol model with the experiment. Required BDC temperature to achieve a certain CA10. ϕ = 0.40, 1200 rpm, and P_{in} = 100 kPa.

As can be seen in Fig. 13, the model $T_{bdc,max}$ matches the experimental T_{bdc} well for CA10 = 364.6°CA. However, as the combustion phasing is changed, the model requires a larger change of T_{bdc} than does the experiment. From this it would be concluded that the model's sensitivity to changes of the charge temperature is not sufficiently high. However, a part of the discrepancy arises from the fact that the experimental wall temperature (T_{wall}) goes up with a more advanced CA10, due to higher PRR and peak-combustion temperatures. With a higher T_{wall}, heat-losses during the compression stroke are reduced slightly. This will contribute to the experimental T_{bdc} curve being less steep than it would have been if T_{wall} could have been kept constant.

To provide a more complete assessment of the fidelity of the mechanism, Fig. 14 compares compressed-gas temperatures at 352°CA as a function of CA10 for the ethanol model and the experiment. This particular crank angle was chosen because it is sufficiently late that most heating due to compression has taken place, but not so late that significant amount of heat has been released. The compressed-gas temperature should also be affected by heat transfer that has occurred up until this crank angle, so any influence of changes to the T_{wall} should be included. First, it should be noted that the experiment and the model are plotted on different y-axes, which are offset by 20K, but with the same total span. This was done to facilitate a comparison of the slopes of the curves. The 20K offset does not necessarily mean that the model predicts ignition temperatures that are too low. It primarily reflects the fact that the 11-zone temperature distribution does not perfectly correspond to the experiment at 352°CA. In particular, by decreasing the size and/or increasing the temperature the cold inactive zone (see Fig. A1), the compressed-gas temperatures could be made to match for the experiment and the model. A comparison of the slopes in Figs. 13 and 14 shows that the model compares more favorably when the temperature just prior to ignition is assessed. Consequently, it can be concluded that the temperature sensitivity of the mechanism is quite good, but slightly less than that of the experiment.

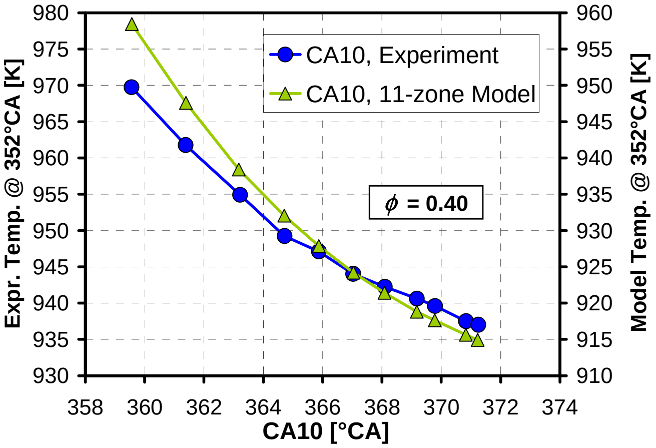

Figure 14. Comparison of the compressed-gas temperature at 352°CA as a function of CA10 for the ethanol model and the experiment.

ENGINE-SPEED SWEEP

It is important to characterize the autoignition reactivity of HCCI fuels across a wide range of engine speeds. Figure 15 shows how the required T_{in} compares for ethanol and gasoline. The supplied $\phi = 0.38$ and T_{in} was adjusted to maintain CA50 = 372°CA as the engine speed was changed. As can be seen, for engine speeds 1200 rpm and higher, the autoignition reactivities of ethanol and gasoline are nearly identical. Furthermore, the HRR profiles are nearly identical, as exemplified for 1500 rpm in Fig. 16.

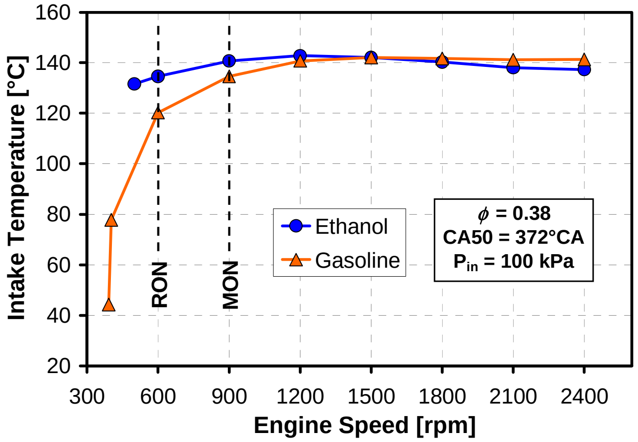

Figure 15. Required T_{in} for maintaining CA50 = 372°CA as engine speed is changed. $\phi = 0.38$ and $P_{in} = 100$ kPa using ethanol and gasoline.

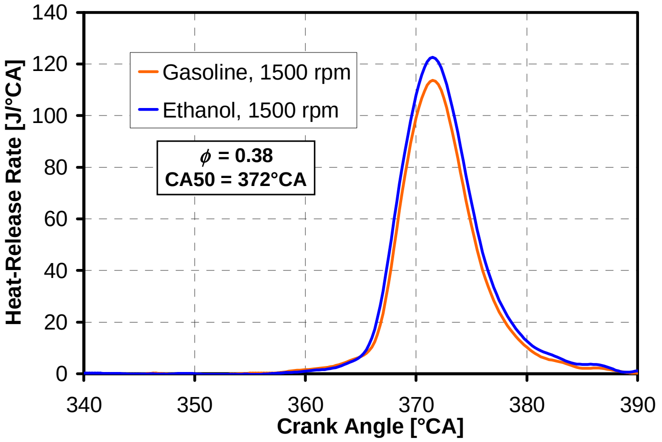

Figure 16. HRR traces for ethanol and gasoline at 1500 rpm. CA50 = 372°CA, $\phi = 0.38$, and $P_{in} = 100$ kPa.

The nearly identical reactivities are perhaps surprising given the different octane numbers of ethanol and gasoline (see Table 3). However, it should be remembered that the RON and MON tests are conducted at 600 and 900 rpm, respectively. Therefore, these test do not directly reveal how reactivities of fuels will compare at higher engine speeds. In fact, a comparison of the data points in Fig. 15 with the RON and MON numbers given in Table 3 reveals that the current HCCI measurements with ethanol and gasoline are consistent with the SI-based RON and MON tests for the same fuels. As can be seen in Fig. 15, when going from higher towards lower speeds the two curves separate some at 900 rpm. At this speed the MON is 89 for ethanol and 83.4 for gasoline, so this is a 5.6 unit difference. At 600 rpm the curves separate even more, which is consistent with the 107 – 90.8 = 16.2 unit difference in RON numbers.

Furthermore, for engine speeds below 600 rpm, the curves separate more distinctly. Near 400 rpm, the points for gasoline fall drastically. This happens because this gasoline starts to develop LTHR, as shown in Fig. 17. In contrast, ethanol remains a single-stage ignition fuel at engine speeds below 600 rpm. The lowest engine speed plotted in Fig. 15 for ethanol is 500 rpm. To determine if ethanol possibly could develop any LTHR when P_{in} = 100 kPa, 300 rpm was also tested using a low T_{in}. However, no tendency to develop LTHR was detected and this supports the assessment that ethanol is a true single-stage ignition fuel.

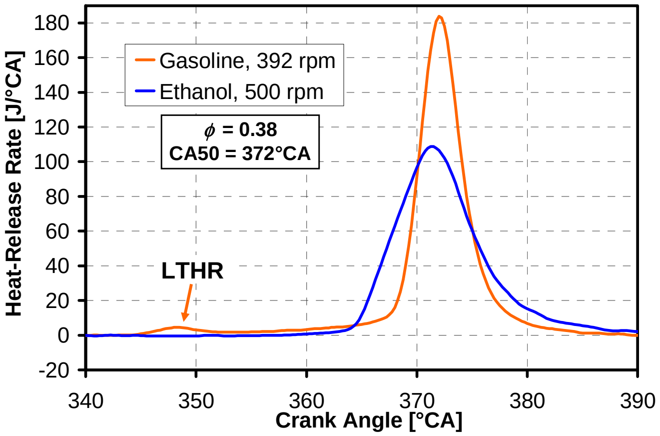

Figure 17. HRR traces for ethanol and gasoline at low speed. CA50 = 372°CA, $\phi = 0.38$ and $P_{in} = 100$ kPa.

Modeling of Engine-Speed Sweep

Figure 18 compares the T_{bdc} requirements for the model and the experiment as engine speed is changed over the 500 – 2400 rpm range. First, it should be noted that the experimental T_{bdc} differs from the experimental T_{in} plotted in Fig. 15 for the reasons discussed previously with respect to Fig. 13. Perhaps the most notable dissimilarity of the trends is that T_{bdc} increases monotonically across the whole engine-speed range in Fig. 18, whereas T_{in} reaches a maximum at 1200 rpm in Fig. 15. The dissimilar trends arise from dynamic heating, which increases strongly with increasing engine speed [27]. The computation of T_{bdc} takes this flow-rate related heating effect into account.

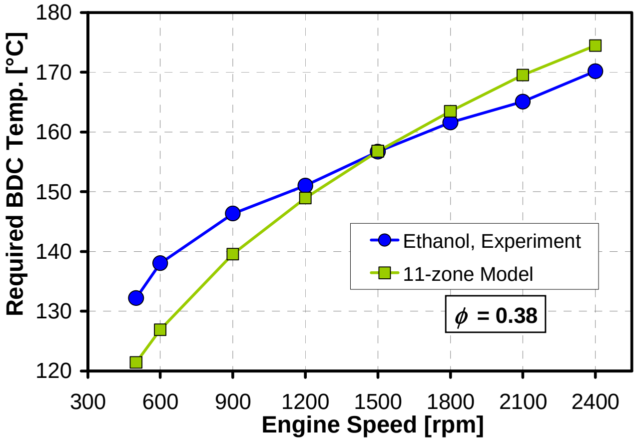

Figure 18. Comparison of the ethanol model with the experiment. Model CA10 is matched to experimental CA10. $\phi = 0.38$, $P_{in} = 100$ kPa.

As can be seen in Fig. 18, at 1500 rpm the T_{bdc} temperatures match nearly perfectly for the model and the experiment. The good match occurred without any tuning of the model, so this indicates that the model predicts well the autoignition reactivity for this operating point. However, there is a difference in slope between the two curves. This indicates that the mechanism is not sufficiently reactive at high engine speeds, and vice versa at low engine speeds. This discrepancy is consistent with the somewhat low temperature sensitivity of the model shown in Figs. 13 and 14. For example, consider the case where the engine speed is doubled from 1200 to 2400 rpm. Operating at double the engine speed means that the autoignition has to take place in only half the time since CA50 was held fixed. To accomplish this experimentally, the T_{bdc} has to be increased by 19°C. However, the model requires 25°C higher temperature to make the hot-ignition point be reached while the available time is cut in half. This difference is conceptually similar to requiring a larger change of T_{bdc} to advance the autoignition timing a certain amount, as shown in Fig. 13.

However, a comparison of T_{bdc} temperatures is not a complete assessment of the fidelity of the mechanism. This is so because with a change of engine speed there is also a change of the time available for heat transfer losses during the compression stroke for the experiment. By studying the compressed-gas temperature just prior to onset of hot ignition, most of the bias due to changes of heat transfer with engine speed can be eliminated. (This is analogous to Fig. 14 for changes of T_{in}.) Consequently, Fig. 19 compares the compressed-gas temperature at 352°CA as a function of engine speed for the ethanol model and the experiment. As can be seen, there is very good agreement of the slopes of the curves. As discussed with respect to Fig. 14, the 20K offset between the experiment and the model can be attributed to the particular thermal distribution used for the model, so the offset should not be interpreted as deficit of the mechanism. Taken together, Figs. 18 and 19 indicate that the mechanism performs well over a wide range of engine speed.

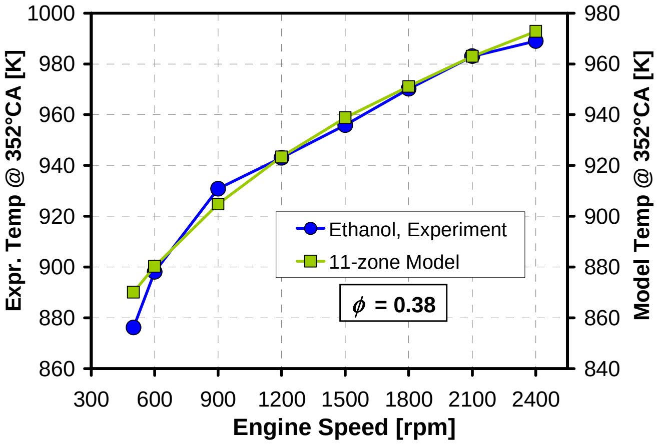

Figure 19. Comparison of the compressed-gas temperature at 352°CA as a function of engine speed for the ethanol model and the experiment.

FUEL/AIR - EQUIVALENCE RATIO SWEEP

Another important fundamental aspect of fuel autoignition chemistry is how the autoignition is affected by changes in ϕ. This is important for the development of engine-control strategies for HCCI engines, but also for SI engines where engine knock due to autoignition in the endgas must be avoided. Unfortunately, it is not easy to measure the isolated effect of changing ϕ on the autoignition timing in an engine. This is because as the amount of fuel is adjusted to change ϕ in a firing engine, the charge temperature at BDC also changes despite T_{in} being held constant. These changes of T_{bdc} occur because the varying amounts of fuel burned affect both in-cylinder wall temperatures (T_{wall}) and residual gas temperatures ($T_{residuals}$), as discussed in [28]. To overcome these effects, the engine could be operated in an alternate-fire mode using direct injection, as demonstrated in [28]. Unfortunately, the fuel-chemistry effect determined with this method includes the effects of fuel vaporization. The vaporization may have a relatively small contribution to the apparent fuel chemistry for fuels like iso-octane and gasoline. However, the latent heat of vaporization for ethanol is substantially higher, so direct injection of fuel should be avoided if possible when measuring only gas-phase chemistry effects.

For these reasons, it was decided to determine the fuel-chemistry effect by a combination of fully-premixed (gas-phase) engine experiments and modeling. Hence, the engine was operated in a manner identical to the preceding sections (and as described in the Experimental Setup section), using the external fuel vaporizer to provide a fully premixed charge of fuel and air to the engine. The intake temperature was held constant at 143°C while data were acquired for ϕ in the 0.38 - 0.44 range. This limited range of ϕ was dictated by the facts that the PRR_{max} becomes unacceptably high for $\phi > 0.44$, and cycle-to-cycle variations become too large for $\phi < 0.38$. The results of this engine operation are shown in Fig. 20.

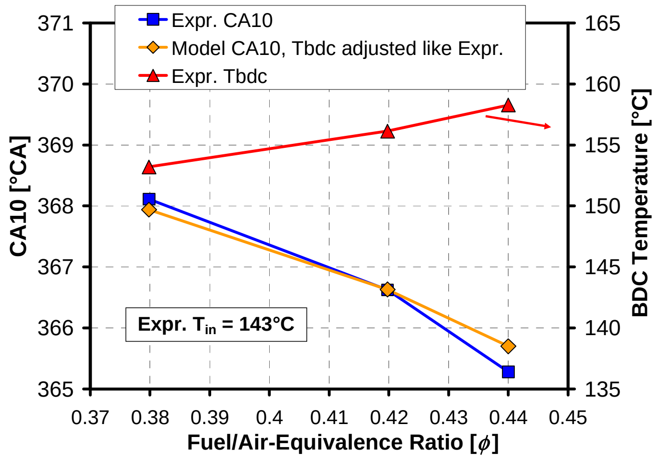

Figure 20. Experimental response of CA10 and T_{bdc} to changes of ϕ while holding T_{in} = 143°C. Model validation with same changes of ϕ and T_{bdc}.

As can be observed, the experimental CA10 advances 2.8°CA across this range of increasing ϕ. Based on this, it appears like the autoignition reactivity is enhanced by increasing ϕ. However, Fig. 20 shows that the experimental T_{bdc} increases by 5°C over the same range of ϕ. This happens primarily because of increased T_{wall} and $T_{residuals}$, as mentioned above.

Based on these results and the limited ϕ-range that could be covered experimentally, it was concluded that modeling is required to determine the true fuel chemistry effects across a wide range of ϕ. However, it is first necessary to validate the model. This was done by examining the response of the model to the identical changes of ϕ and T_{bdc} as the experiment. The results of these computations are also plotted in Fig. 20. It can be seen that CA50 of the model advances by 2.2°CA across this range of increasing ϕ. This is slightly less than the 2.8°CA advancement for the experiment. A part of this small discrepancy is likely due to the insufficient T_{bdc} sensitivity of the model, as discussed in conjunction with Fig. 13. Overall, the model does a good job in capturing the advancing combustion phasing with increasing ϕ and T_{bdc}, so for the purpose of this section, the model can be considered successfully validated.

Additional computations were performed to determine the true fuel chemistry effects of changing ϕ across a wide range of ϕ while holding $T_{bdc,max}$ = constant = 152°C. The results are plotted in Fig. 21 together with the three validation points from Fig. 20. The results are quite remarkable. With the effects of changing T_{wall} and $T_{residuals}$ removed, the response to changes in ϕ reverses. (A similar reversal of the trends was observed for iso-octane in Ref. [28], using an alternate-fire operating mode.)

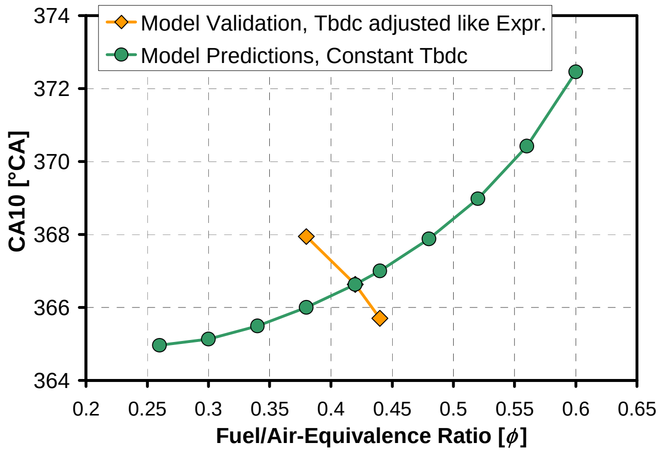

Figure 21. Model prediction of CA10 as ϕ changes for constant $T_{bdc,max}$ = 152°C. Gas-phase only. Validation data are reproduced from Fig. 20. 1200 rpm and P_{in} = 100 kPa.

To provide insights as to why the autoignition of ethanol is retarded with increasing ϕ, Fig. 22 plots the temperature traces for ϕ = 0.31 and 0.62. As can be seen, the compressed-gas temperature 5°CA before TDC is 47 K lower for the higher-ϕ case. This is a thermodynamic effect caused by a higher heat-capacity of the charge, leading to a lower ratio of specific-heat capacities (lower γ). This is a well-known cooling effect that regularly is used to suppress engine knock at high loads in SI gasoline engines by operating the engine rich of stoichiometric [29].

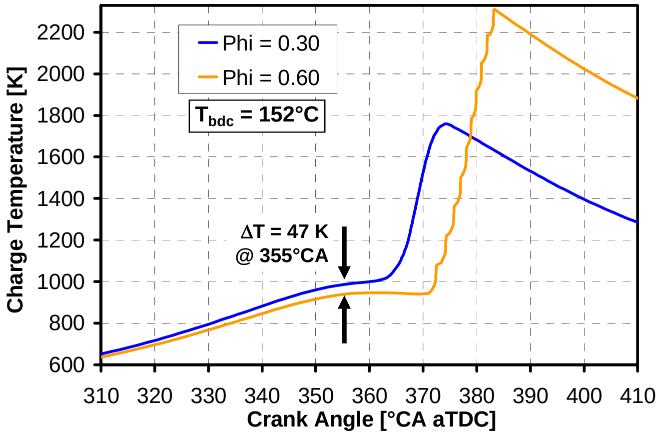

Figure 22. Model prediction of temperature traces for operation with $T_{bdc,max}$ = const = 152°C with ϕ = 0.31 and 0.62. 1200 rpm, and P_{in} = 100 kPa.

There are reasons to believe that the autoignition-suppression effect resulting from thermodynamic cooling is greater for ethanol than for traditional non-oxygenated fuels like gasoline. (For the following example, iso-octane serves as a gasoline surrogate since its thermodynamic properties are more accurately known.) First, the stoichiometric air/fuel ratio is much lower for ethanol; 9.0 vs. 15.1 for iso-octane. As Fig. 23 shows, this requires 68% more fuel mass to be supplied for the same operating point. Ethanol has substantially lower mass-specific heat capacity than iso-octane, as Fig. 24 shows. Nonetheless, because the amount of fuel is 68%

greater, the total heat capacity of the fuel becomes 33% higher than for iso-octane for the same ϕ. (The heat capacities of the two fuels were computed for a temperature of 700 K, which is roughly half-way between T_{bdc} and the ignition temperature.) This fact, combined with the high temperature sensitivity of ethanol autoignition (see Fig. 2), explains why Fig. 21 shows such a strong retarding effect for increasing ϕ.

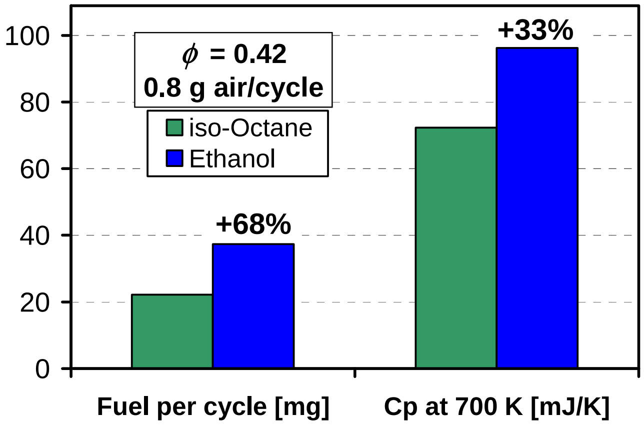

Figure 23. Illustration of differences in fueling rate and heat-capacity of the fuel between iso-octane and ethanol.

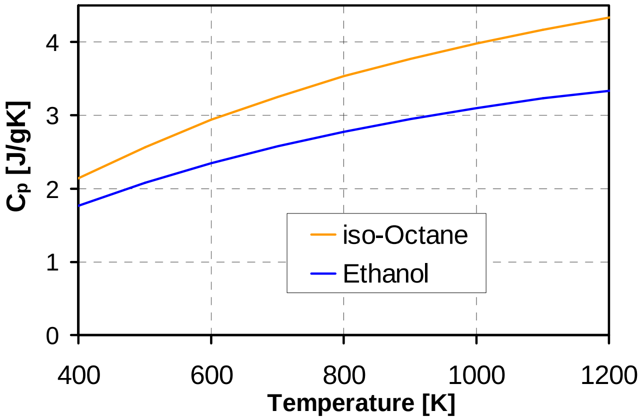

Figure 24. Mass-specific heat-capacity of iso-octane and ethanol as a function of temperature. Data from NIST Chemistry WebBook [30].

The more retarded CA10 with increasing ϕ has practical implications. For example, if an HCCI engine is operated such that occasional misfire cycles occur, quickly increasing the fueling rate of ethanol will likely create a higher frequency of misfire cycles rather than stabilizing the combustion.

INTAKE-PRESSURE BOOST SWEEP

Since the HCCI combustion process is dilute in comparison with traditional stoichiometric SI combustion, the upper load limit of HCCI is lower than for SI for a given P_{in} [3,18,31]. Therefore, to reach BMEP values that are comparable with naturally-aspirated SI engines, intake-pressure boost is required. Furthermore, one of the current strong trends within the light-duty automotive industry is the downsizing of SI engines in order to reduce overall vehicle fuel consumption. Engine downsizing often encompasses the application of high intake-pressure boost, and knock-suppressing benefits of ethanol have been observed for such boosted operation [5]. For these reasons, it is important to characterize the autoignition chemistry of ethanol over a wide range of intake pressures. This also provides an opportunity for validation of the chemical-kinetics mechanism for ethanol, which would allow modeling to aid the development of high-output HCCI and SI engines.

In order to generate a reference data set, the engine was operated at 1200 rpm with a constant $\phi = 0.40$ while holding CA10 = 369.0°CA as P_{in} was changed. Some of the pressure traces from this data set are shown in Fig. 25. The timing of CA10 is marked with a vertical dashed line. In order to maintain CA10 = 369.0°CA as P_{in} was increased, T_{in} had to be decreased. The corresponding reduction of T_{bdc} is plotted with blue circles in Fig. 26.

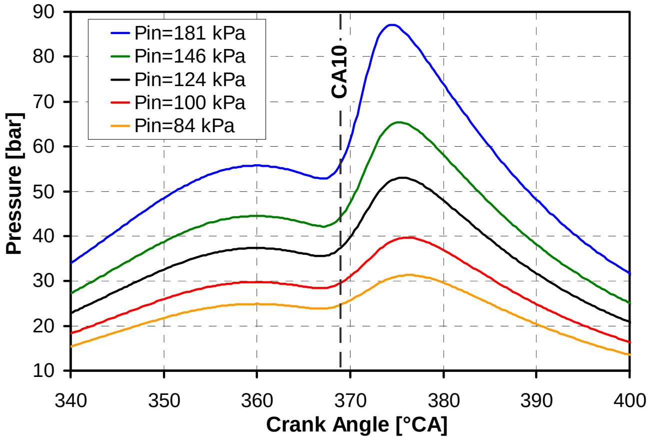

Figure 25. Pressure traces for ethanol for P_{in} = 84 – 181 kPa. CA10 = 369.0°CA, $\phi = 0.40$ and 1200 rpm.

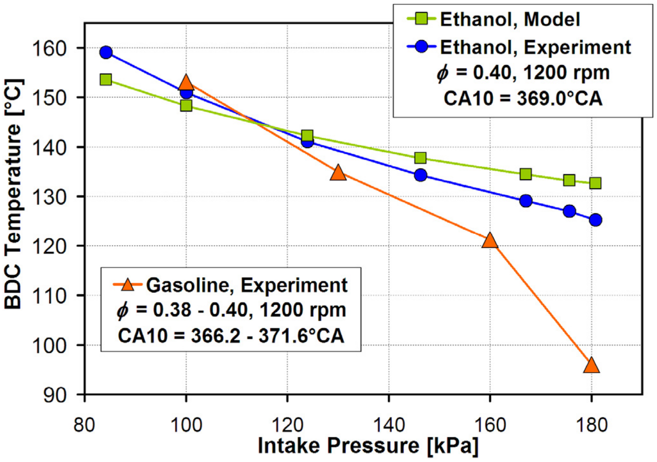

Figure 26. Experimental and model results for ethanol, showing required BDC temperature to maintain CA10 = 369.0°CA as P_{in} changes. Experimental results for gasoline from Ref. [32] are shown for comparison.

Figure 26 shows that only a modest enhancement of the autoignition reactivity occurs as P_{in} is increased. Compensating for a 115% increase of P_{in} from 84 to 181 kPa only requires a modest reduction of T_{bdc} of 34°C.

In addition, a portion of these 34°C can be attributed to lower influence of heat transfer during the intake and compression strokes for a higher-density charge. Thus, the actual enhancement of the autoignition reactivity with intake boost is somewhat less than Fig. 26 indicates. To better understand why only a modest enhancement of the autoignition reactivity is observed with increasing P_{in}, Fig. 27 plots the early HRR traces for a range of intake pressures. As can be seen, essentially no exothermic heat-releasing reactions occur until 355°CA. Beyond this point, the HRR gradually increases until hot ignition occurs around 366°CA. The HRR traces have been normalized by the total amount of detected heat release in order to eliminate differences between the HRR traces caused solely by an increase of the total amount of fuel burned as P_{in} is increased. (For reference, the peak HRR falls in the 10 – 19%/°CA range, depending on P_{in}.) With this normalization, the HRR traces are very similar and ethanol shows no tendency to develop LTHR or enhanced ITHR as P_{in} is increased. This finding is in agreement with the work of Christensen et al. [6]. Despite operating their engine with P_{in} up to 300 kPa, ethanol maintained its clear single-stage autoignition characteristics.

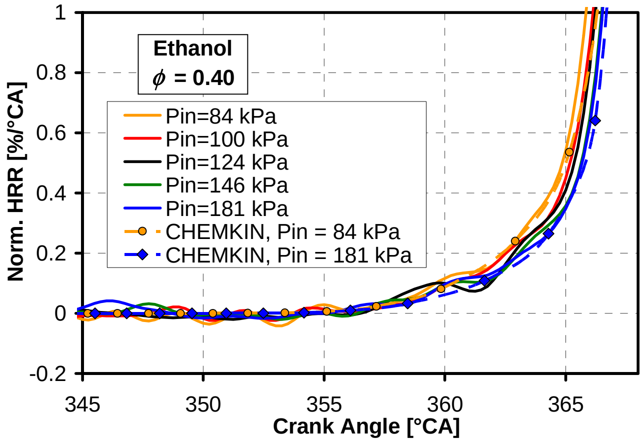

Figure 27. Early HRR for P_{in} = 84 – 181 kPa, using ethanol. CA10 ≈ 369.0°CA, ϕ = 0.40 and 1200 rpm.

This behavior of ethanol is in sharp contrast with that of gasoline, which shows a marked increase of the ITHR as P_{in} is increased. Figure 28 demonstrates this effect for gasoline. For the lowest P_{in} of 100 kPa, the HRR trace does not start to curve up until 355°CA, which is similar to ethanol. However, for the higher intake pressures it is clear that the heat release starts earlier and also results in substantially more ITHR. The highest P_{in} of 180 kPa even starts to show a tendency for LTHR. Correspondingly, Fig. 26 shows that the T_{bdc} requirement for gasoline drops much more quickly with increasing P_{in} than for ethanol. The reduction in T_{bdc} is particularly strong between P_{in} = 160 and 180 kPa as gasoline develops some amount of LTHR. Finally, it should be noted that the gasoline data plotted in Figs. 26 and 28 were not acquired as a reference data set with constant ϕ and CA10. More details of this boosted HCCI operation using gasoline can be found in a concurrent study by Dec and Yang [32].

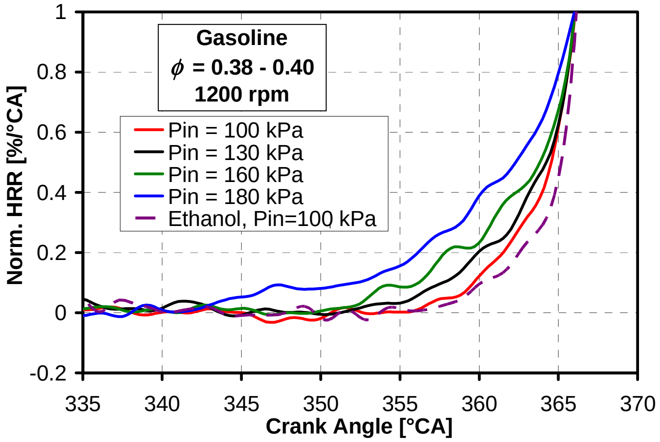

Figure 28. Gasoline results showing the development of enhanced ITHR with increasing P_{in}. CA10 ≈ 367°CA, $\phi \approx 0.38$ and 1200 rpm [32]. The ethanol P_{in} = 100 kPa curve from Fig. 27 is reproduced for reference.

Modeling of intake-pressure boost sweep

The chemical kinetics mechanism was evaluated against the reference P_{in} sweep and the results are plotted in Fig. 26 together with the experimental results discussed above. The model matches the experiment well for P_{in} ≈ 120 kPa. However, across the P_{in} range covered, the $T_{bdc,max}$ for the model has to be adjusted only 21°C, whereas the experimental T_{bdc} has to be adjusted 34°C. A part of this discrepancy, if not all of it, can be explained by reduced influence of heat-transfer on the gas temperature for operation with high P_{in}, as mentioned above. To provide a more complete assessment, Fig. 29 compares the compressed-gas temperature at 350°CA (T_{350}) as a function of P_{in} for the ethanol model and the experiment. As can be seen, the data now suggest that the mechanism has a pressure sensitivity that is higher than the experiment. Thus, given the uncertainties associated with both ways of assessing the model (T_{bdc} or T_{350}), the mechanism seems to have a pressure sensitivity that is close to the experiment. Further examination of the model results provides additional evidence that the mechanism performs well across wide ranges of P_{in}, as discussed below.

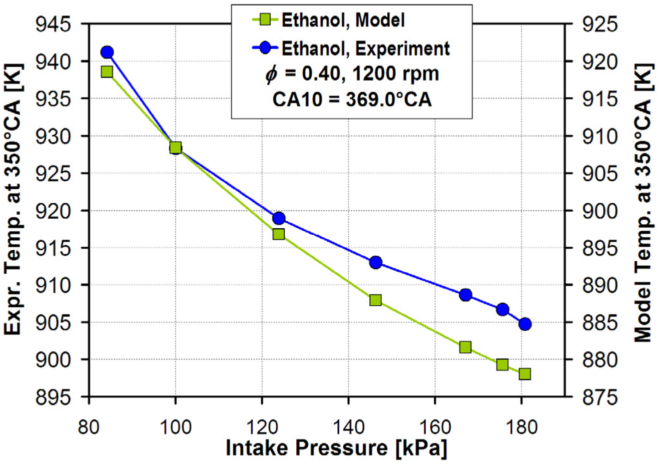

Figure 29. Comparison of the compressed-gas temperature at 352°CA as a function of intake pressure for the ethanol model and the experiment.

In Fig. 27, two HRR traces for the model at P_{in} = 84 and 181 kPa are plotted (curves with symbols). The onset of significant HRR occurs at 356°CA, which is identical to the experiment. The rate of increase of the HRR during the early part of the combustion event is also nearly identical to the experiment. Furthermore, Fig. 27 shows that higher P_{in} does not increase the ITHR for the model, which corresponds well to the experimental observation. On the contrary, the model's ITHR is slightly lower for the higher P_{in} case. This could be caused by the somewhat lower $T_{bdc,max}$ and T_{350} for the higher P_{in} case. Further insights of how autoignition and combustion proceed differently at different P_{in} can be obtained by plotting the normalized HRR of the hottest zone against its temperature, as shown in Fig. 30. The autoignition and combustion proceed from lower to higher temperatures in this graph. Examination of the curves reveals that for the P_{in} = 84 kPa case, significant HRR (>0.1%/°CA) commences when the charge has been compressed to around 1000 K. In contrast, the higher P_{in} = 181 kPa case starts to show significant heat release already at 960 K. Once underway, the early heat release in the 1000 – 1400 K range progresses at a much higher rate for the higher-P_{in} case. These observations demonstrate some differences in the autoignition process that arise when P_{in} is changed, and can be used as a starting point for further investigations

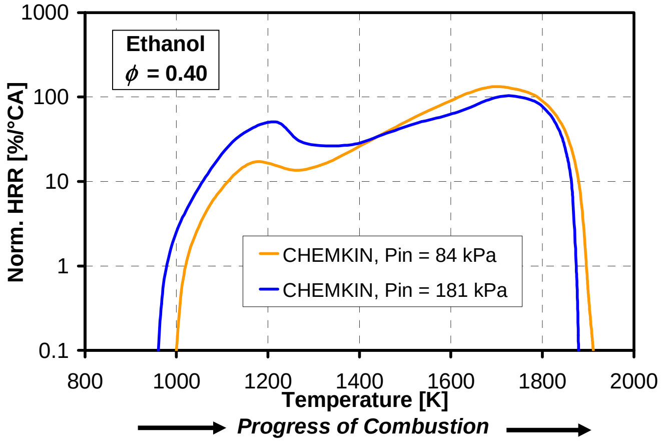

Figure 30. Comparison of predicted HRR of the hottest zone as a function of temperature for P_{in} = 84 and 181 kPa, corresponding to the model results in Fig. 24.

DEMONSTRATION OF HIGH LOAD

Since it is important to be able to operate in HCCI mode over a large load range, it is of interest to determine the IMEP limits for operation with ethanol. However, a comprehensive investigation of this is beyond the scope of the current study. Nonetheless, to demonstrate operation with a relatively high IMEP and some of the issues associated with high-load operation, some additional measurements were performed. First, however, the load range for the reference data set with intake boost is examined.

The yellow circles in Fig. 31a show the range of $IMEP_g$ covered in the reference data set, for which CA10 = 369.0°CA was maintained. It can be seen that $IMEP_g$ = 8.8 bar is reached at P_{in} = 181 kPa. At this point, Fig. 31b shows that the ringing intensity [33] is slightly below the 5 MW/m^2 limit that has been established previously for this engine [19]. The ringing intensity increases with P_{in}, partly because the total pressure rise during combustion increases, and partly because the 10-50% burn duration shortens. The burn duration shortens because with CA10 held fixed, CA50 advances with higher P_{in}, as illustrated with black circles in Fig. 31b. The reason why higher P_{in} was not tested is that beyond P_{in} = 181 kPa, control of the combustion phasing is lost and combustion-phasing run-away occurs.

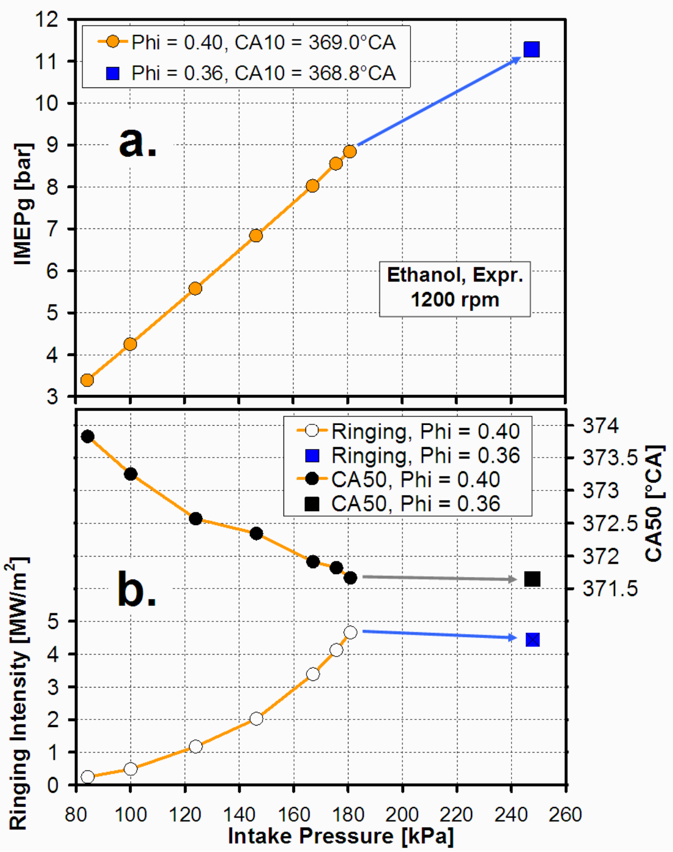

Figure 31. IMEP$_g$, ringing, and CA50 for intake boost reference data set and additional higher P$_{in}$ – lower ϕ operation.

Figure 32 illustrates the run-away sequence. The green dots represent CA50 of the individual cycles and a black curve is fit to the data to illustrate the trend. As can be seen, the average CA50 is first relatively stable but then starts to slowly drift to more advanced CA50 in the 30 – 240 s time range. This drift of CA50 is accompanied by a slight increase of the measured firedeck temperature. Then at 300 s a transition to a more rapid run-away occurs and within two minutes CA50 has advanced strongly. Associated with the advancing CA50 is a large increase of the firedeck temperature due to increased convective heat-transfer as a result of excessive ringing and in-cylinder gas oscillations [19,34]. These are typical characteristics of wall-heating-induced run-away, as discussed in previous publications [3,19,31].

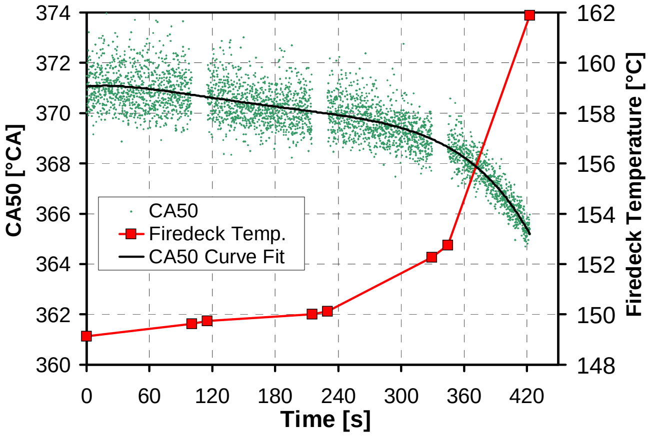

Figure 32. Wall-heating induced run-away of the combustion phasing for operation with $\phi = 0.40$ and P_{in} = 182 kPa.

In general, one of the reasons that wall-heating induced run-away occurs is that the autoignition timing is overly sensitive to changes of the compressed-gas temperature. As discussed in conjunction with Fig. 2, CA50 of ethanol is sensitive to changes of T_{in}, partly because of ethanol's pronounced single-stage ignition characteristics with very little ITHR. The single-stage ignition characteristics lead to particularly low TRR prior to the main combustion when hot ignition occurs late relative to TDC. This is the situation for the highest load point in the reference data set, as the gold curve in Fig. 33 shows. As can be seen, the TRR is even negative in the 362 - 365°CA range as piston-expansion cooling and heat-transfer losses exceed the (mass-averaged) temperature rise due to autoignition reactions. (The temperature of the hottest in-cylinder zone is expected to increase monotonically, however.) The TRR becomes positive again at 365°CA, just before hot ignition occurs. The high temperature sensitivity of the hot-ignition timing associated with a low TRR contributes to the risk of wall-heating induced run-away.

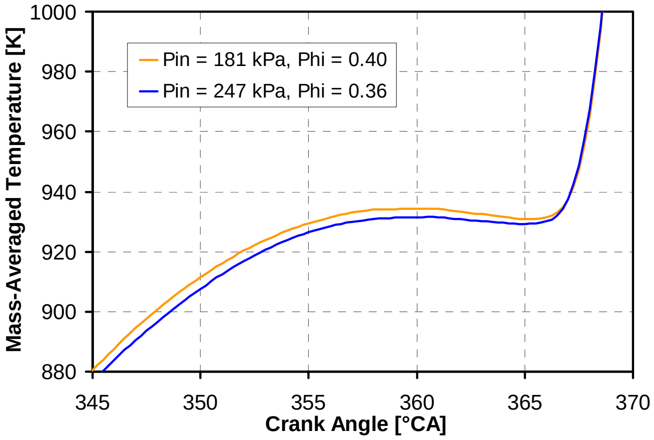

Figure 33. Temperature traces for operation with $\phi = 0.40$ at P_{in} = 181 kPa (gold), and with $\phi = 0.36$ at P_{in} = 247 kPa (blue).

There are several options for reaching an $IMEP_g$ higher than 8.8 bar. The engine can for example be operated with:

1. $\phi > 0.40$ at P_{in} = 181 kPa.

2. $\phi = 0.40$ at $P_{in} > 181$ kPa.
3. $\phi < 0.40$ at $P_{in} >> 181$ kPa.

Options 1 and 2 would both require CA10 to be more retarded than 369.0°CA in order to maintain a ringing intensity below 5 MW/m^2. This would lead to a TRR that is even lower than for the $IMEP_g = 8.8$ bar data point. Hence, the risk of wall-heating induced run-away (or retard to misfire) may increase since the lower TRR would lead to a higher temperature sensitivity of the hot-ignition timing. Because of these considerations, it was decided to pursue option 3 instead. With a lower ϕ of 0.36 and a substantially higher P_{in} of 247 kPa, the hot-ignition point could be advanced by 0.2°CA. This resulted in a somewhat higher TRR, as illustrated with the blue curve in Fig. 33, and also a lower tendency for run-away. Thanks to the substantially higher intake pressure, a marked increase of $IMEP_g$ could be achieved.

As represented by the squares in Fig. 31, by operating the engine with $\phi = 0.36$ and $P_{in} = 247$ kPa, an $IMEP_g$ of 11.3 bar was reached while maintaining an acceptable ringing intensity. This data point does not indicate where the high-load limits are, but rather illustrates one way of operating the engine to reach a relatively high IMEP. Further work is needed to determine the best way to obtain high IMEP and also the operational limits of such high-load operation, including the possibility for using a turbocharger to obtain the required intake boost pressure.

SUMMARY AND CONCLUSIONS

Neat ethanol works well as an HCCI fuel and maintains single-stage ignition characteristics for all tested operating points, including high intake pressures. One potential advantage is:

- Only small adjustments of T_{in} are required to compensate for large changes of engine speed and intake-pressure boost.

However, ethanol exhibits low temperature-rise rates prior to the main combustion. This may have some disadvantages:

- The amount of useful CA50 retard is expected to be limited and this could hamper the ability to control PRR_{max}/knock at high loads.

Furthermore, no enhancement of autoignition with increasing fuel/air equivalence ratio was observed. One potential advantage of this is:

- Only relatively small adjustments of T_{in} will be required when engine load is changed.

One potential disadvantage:

- Increased fueling will not help to quickly recover stable ignition for a misfiring HCCI engine.

The newly developed chemical-kinetics mechanism for ethanol performs very well, and the predicted autoignition reactivity of ethanol matches well the experiment. Using a 11-zone model, the sensitivities of the mechanism to changes of engine speed or intake-pressure boost were assessed and found to be in good agreement with the experiment. However, the sensitivity of the mechanism to changes of the charge temperature appears to be slightly too low.

REFERENCES

1. Maly R.R., Degen, W., “Impact of Future Fuels,” SAE Technical Paper 2002-21-0073, 2002.

2. Yun, H., Wermuth, N., and Najt, P., “Development of Robust Gasoline HCCI Idle Operation Using Multiple Injection and Multiple Ignition (MIMI) Strategy,” SAE Technical Paper 2009-01-0499, 2009.

3. Sjöberg, M. and Dec, J.E., “Influence of Fuel Autoignition Reactivity on the High-Load Limits of HCCI Engines,” SAE Technical Paper 2008-01-0054, 2008.

4. Sjöberg, M. and Dec, J.E., “Comparing Late-cycle Autoignition Stability for Single- and Two-Stage Ignition Fuels in HCCI Engines,” *Proceedings of the Combustion Institute* **31**: 2895–2902, 2007.

5. Christie, M.J., Fortino, N., and Yilmaz H., ”Parameter Optimization of a Turbo Charged Direct Injection Flex Fuel SI Engine,” SAE Technical Paper 2009-01-0238, 2009.

6. Christensen, M., Johansson, B., Amnéus, P., and Mauss, F., “Supercharged Homogeneous Charge Compression Ignition,” SAE Technical Paper 980787, 1998.

7. Gnanam, G., Sobiesiak A., Reader, G., and Zhang C., “An HCCI Engine Fuelled with Iso-octane and Ethanol,” SAE Technical Paper 2006-01-3246, 2006.

8. Zhang, Y., He, B.-Q., Xie, H., and Zhao H., “The Combustion and Emission Characteristics of Ethanol on a Port Fuel Injection HCCI Engine,” SAE Technical Paper 2006-01-0631, 2006.

9. Dec, J.E. and Sjöberg, M., “A Parametric Study of HCCI Combustion – the Sources of Emissions at Low Loads and the Effects of GDI Fuel Injection,” SAE Technical Paper 2003-01-0752, 2003.

10. Heywood, J.B., “Internal Combustion Engine Fundamentals,” McGraw-Hill, New York, ISBN 0-07-100499-8, 1988.

11. Dec, J.E, Davisson, M.L., Sjöberg, M., Leif, R.N., and Hwang, W., “Detailed HCCI Exhaust Speciation and the Sources of Hydrocarbon and Oxygenated Hydrocarbon Emissions,” SAE Technical Paper 2008-01-0053, 2008.

12. Sjöberg, M., Dec, J.E., and Cernansky, N.P., “Potential of Thermal Stratification and Combustion Retard for Reducing Pressure-Rise Rates in HCCI Engines, based on Multi-Zone Modeling and Experiments,” SAE Technical Paper 2005-01-0113, 2005.

13. Lutz, A. E., Kee, R. J., and Miller, J. A., “Senkin: A FORTRAN Program for Predicting Homogeneous Gas Phase Chemical Kinetics with Sensitivity Analysis,” Sandia National Laboratories Report No. SAND87-8248.

14. Lutz, A.E., “Multi-zone Model for Homogeneous Ignition,” Sandia National Laboratories, Internal Report, July 8, 2002.

15. Curran H., Serinyel, Z., and Metcalfe, W., Combustion Chemistry Centre at NUI Galway, Ireland, personal communication, 2009.

16. Mehl, M., Pitz, W.J., Sjöberg, M., and Dec, J.E., "Detailed Kinetic Modeling of Low-Temperature Heat Release for PRF Fuels in an HCCI Engine," SAE Technical Paper 2009-01-1806, 2009.

17. Christensen, M., Hultqvist, A., and Johansson, B., "Demonstrating the Multi Fuel Capability of a Homogeneous Charge Compression Ignition Engine with Variable Compression Ratio," SAE Technical Paper 1999-01-3679, 1999.

18. Urushihara, T., Hiraya, K., Kakuhou, A., and Itoh, T., "Parametric Study of Gasoline HCCI with Various Compression Ratios, Intake Pressures and Temperatures," presented at A New Generation of Engine Combustion Processes for the Future ? :77 - 84, France, Nov. 26-27, 2001.

19. Sjöberg, M., Dec, J.E., Babajimopoulos, A., and Assanis, D., "Comparing Enhanced Natural Thermal Stratification against Retarded Combustion Phasing for Smoothing of HCCI Heat-Release Rates," SAE Technical Paper 2004-01-2994, 2004.

20. Dec, J.E., and Hwang, W., "Characterizing the Development of Thermal Stratification in an HCCI Engine Using Planar-Imaging Thermometry," SAE Technical Paper 2009-01-0650, 2009.

21. Sjöberg, M. and Dec, J. E., "An investigation into lowest acceptable combustion temperatures for hydrocarbon fuels in HCCI engines," *Proceedings of the Combustion Institute* **30**:2719 – 2726, 2005.

22. Jun, D. and Iida, N., "A Study of High Combustion Efficiency and Low CO Emission in a Natural Gas HCCI Engine," SAE Technical Paper 2004-01-1974, 2004.

23. Aceves S.M., Flowers, D.L., Espinosa-Loza, F., Martinez-Frias, J., Dec, J.E., Sjöberg, M., Dibble R.W., and Hessel, R.P., "Spatial Analysis of Emissions Sources for HCCI Combustion at Low Loads Using a Multi-Zone Model," SAE Technical Paper 2004-01-1910, 2004.

24. Christensen, M., Hultqvist, A., and Johansson, B., "The Effect of Top-land Geometry on Emissions of Unburned Hydrocarbons from a Homogeneous Charge Compression Ignition (HCCI) Engine," SAE Technical Paper 2001-01-1893, 2001.

25. Aceves, S. M., Flowers, D. L., Espinosa-Loza, F., Martinez-Frias, J., Dibble, R. W., Christensen, M., Johansson, B., and Hessel, R. P., "Piston-Liner Crevice Geometry Effect on HCCI Combustion by Multi-Zone Analysis," SAE Technical Paper 2002-0-2869, 2002.

26. Babajimopoulos, A., Lavoie, G.A., and Assanis, D.N., "Modeling HCCI Combustion with High Levels of Residual Gas Fraction – A Comparison of Two VVA Strategies," SAE Technical Paper 2003-01-3220, 2003.

27. Sjöberg, M. and Dec, J.E., "An Investigation of the Relationship between Measured Intake Temperature, BDC Temperature, and Combustion Phasing for Premixed and DI HCCI Engines," SAE Technical Paper 2004-01-1900, 2004.

28. Dec, J.E. and Sjöberg, M., "Isolating the Effects of Fuel Chemistry on Combustion Phasing in an HCCI Engine and the Potential of Fuel Stratification for Ignition Control," SAE Technical Paper 2004-01-0557, 2004.

29. Grandin, B., Denbratt, I., Bood, J., Brackmann, C., Bengtsson, P.-E., "A Study of the influence of exhaust gas recirculation and stoichiometry on the heat release in the end-gas prior to knock using rotational coherent anti-Stokes Raman spectroscopy thermometry," *Int. J. of Engine Research* **3**(4):209-221, 2002.

30. NIST Chemistry WebBook, “Standard Reference Database Number 69,” March 2009, http://webbook.nist.gov/chemistry/

31. Olsson, J.-O., Tunestål, P., Johansson, B., Fiveland, S., Agama, J.R., and Assanis, D.N., “Compression Ratio Influence on Maximum Load of a Natural Gas-Fueled HCCI Engine,” SAE Technical Paper 2002-01-0111, 2002.

32. Dec, J.E., and Yang, Yi, ”Boosted HCCI for High Power without Engine Knock and with Ultra-Low NO_x Emissions – using Conventional Gasoline,” SAE Technical Paper 2010-01-1086.

33. Eng, J.A., "Characterization of Pressure Waves in HCCI Combustion,” SAE Technical Paper 2002-01-2859, 2002.

34. Tsurushima, T., Kunishima, E., Asaumi Y., Aoyagi, Y., and Enomoto, Y., "The Effect of Knock on Heat Loss in Homogeneous Charge Compression Ignition Engines,” SAE Technical Paper 2002-01-0108, 2002.

CONTACT INFORMATION

Corresponding author’s mailing address: Magnus Sjöberg, Sandia National Laboratories, MS 9053, PO Box 969, Livermore, CA 94551-0969, USA.

ACKNOWLEDGMENTS

The authors would like to thank Yi Yang for help with heat-release calculations and Richard Steeper for valuable suggestions for the manuscript. Thanks also to Gary Hux, Kenneth St. Hilaire, Chris Carlen, and Gary Hubbard for their dedicated support of the HCCI laboratory.

The work was performed at the Combustion Research Facility, Sandia National Laboratories, Livermore, CA. Financial support was provided by the U.S. Department of Energy, Office of Vehicle Technologies. Sandia is a multiprogram laboratory operated by the Sandia Corporation, a Lockheed Martin Company, for the United States Department of Energy's National Nuclear Security Administration under contract DE-AC04-94AL85000.

APPENDIX A: THERMAL DISTRIBUTION FOR MULTI-ZONE MODEL AND COMPARISON WITH 1-ZONE MODEL

The purpose of the multi-zone modeling presented in the main body of the paper is to evaluate the accuracy of a newly developed chemical-kinetics mechanism for ethanol. The pressure-rise rate during combustion is made to approximate that of the experiment by initializing ten active zones with different temperatures, for a total thermal width of 25K at BDC (TW_{bdc}), as illustrated in Fig. A1. To make the total pressure rise during combustion better match that of the experiment, the 11th “inactive” zone is initialized sufficient cold at BDC so that it never ignites. This zone represents 16% of the total in-cylinder mass, as illustrated in Fig. A1. This 16% accounts for combustion inefficiencies and heat-transfer (and to a lesser extent blow-by) on the pressure rise during combustion. The inactive zone is needed since the model is adiabatic and does not include heat-transfer, as discussed in more detail in Ref. [12].

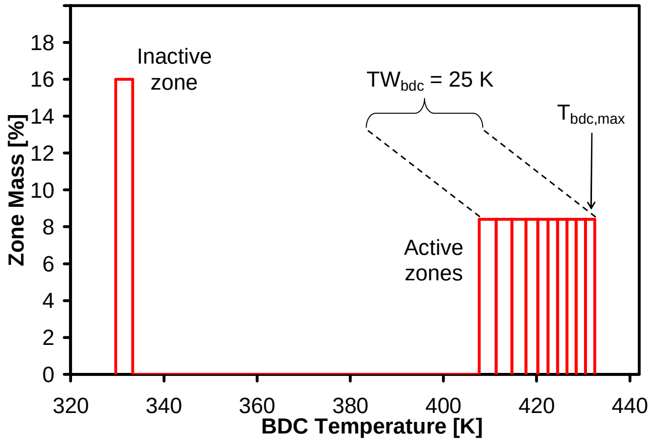

Figure A1. Illustration of the zone distribution used for the 11-zone model.

The TW$_{bdc}$ of 25 K is larger than some of the previous modeling of the same engine [12]. The larger TW arises because the thermal spacing between the five coldest active zones was increased somewhat in order to improve the pressure match between the model and the experiment during the latter part of the combustion event. The experimental CA10 = 363.2°CA operating point in Fig. 12 is the case against which the model was compared when selecting the thermal distribution of the model. Indeed, Fig. 12 shows that the chosen temperature distribution makes the pressures during combustion match very well.

The chosen thermal spacing between the colder zones is also justified by the shape of the in-cylinder thermal distribution. Plotted in Fig. A2 is the result from a KIVA simulation, reproduced from Ref. [19]. Also plotted are the zone temperatures at 365°CA for the current 11-zone model, corresponding to the CA10 = 363.2°CA case in Fig. 12. Both the presented cases in Fig. A2 include fuel, but the combustion is turned off to clearly see the thermal distribution without the temperature rise due to heat release. For the KIVA run, the resulting thermal distribution near TDC is the result of heat-transfer processes during the compression stroke, since a thermally homogeneous charge was initialized at BDC for the CFD calculation. It can be seen that the thermal distributions of the 60% hottest in-cylinder mass are reasonably similar for KIVA and the current multi-zone.

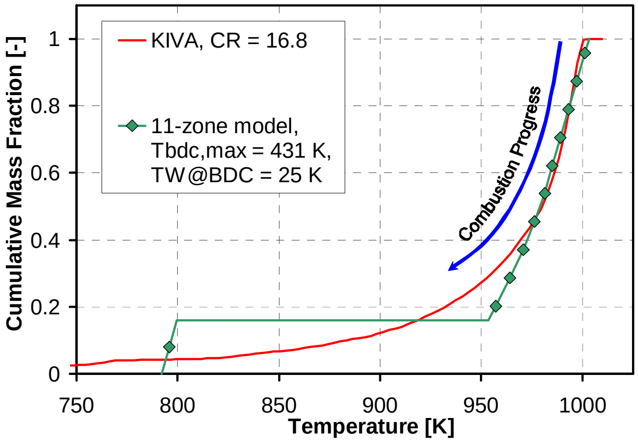

Figure A2. Comparing cumulative temperature at 365°CA for the 11-zone model, and KIVA results from Ref. [19] using CR = 16.8. Reactions turned off. The symbols represent each individual zone temperature.

Also, the more retarded case in Fig. 12 has a good pressure match until well past the CA10 point of 369.2°CA. Hence, the chosen thermal distribution should serve well for capturing the timing of CA10, and probably also for CA50. CA10 is the burn point for which the evaluation of the mechanism takes place in the main body of the paper. To also capture well the end of combustion and, for example, the 10 – 90 % burn duration, an adjustment of the thermal width and the size of the inactive zone would have been necessary for the more retarded case. A need for adjustment of the thermal distribution would probably be needed also for capturing well the end of combustion for other operating points, like higher or lower speed, and boosted operation.

To put the current multi-zone approach to mechanism evaluation in context, Fig. A3 presents a comparison between the 11-zone model (reproduced from Fig. 13) and a much more simple 1-zone model that is based on the Senkin application of CHEMKIN III [13]. The 1-zone model can be thought of as representing the close-to-adiabatic core in the experiment. Since KIVA predicts that the hottest 20% of the compressed gas has a fairly uniform temperature, the 50% burn point of the 1-zone model corresponds roughly to CA10 of the overall combustion event. Based on this, T_{bdc} of the single-zone model was adjusted so its CA50 matched the experimental CA10. For the multi-zone model, the BDC temperature of the hottest zone ($T_{bdc,max}$, see Fig. A1) was adjusted until the CA10 of the model matched the experimental CA10. This approach for the multi-zone model is justified by the fact that the model and experiment have very similar pressure histories, at least until CA10, as Fig. 12 shows. With a similar pressure history, the hottest zone in the model also has a temperature history that is similar to the hottest (and almost adiabatic [26]) portion of the core of the experiment). As can be seen, the results are very similar for the two modeling approaches. From this it can be concluded that a 1-zone approach can be sufficiently accurate if the model is compared against the experimental CA10. However, for matching the model against CA50 or for studying burn durations, some kind of multi-zone approach would be needed to capture the effects of naturally occurring in-cylinder thermal stratification.

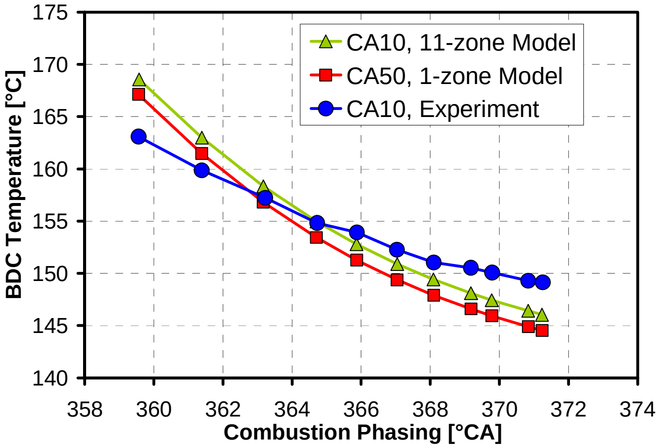

Figure A3. Comparison of both the 1-zone and 11-zone ethanol models with the experiment. Required BDC temperature to achieve a certain CA10. $\phi = 0.40$, 1200 rpm, and $P_{in} = 100$ kPa.